



HAL
open science

Deep Eddy Kinetic Energy in the Tropical Pacific from Lagrangian Floats

A. Delpech, S. Cravatte, F. Marin, C. Ménesguen, Yves Morel

► **To cite this version:**

A. Delpech, S. Cravatte, F. Marin, C. Ménesguen, Yves Morel. Deep Eddy Kinetic Energy in the Tropical Pacific from Lagrangian Floats. *Journal of Geophysical Research. Oceans*, 2020, 125 (8), 10.1029/2020JC016313 . hal-03001963

HAL Id: hal-03001963

<https://hal.science/hal-03001963>

Submitted on 12 Nov 2020

HAL is a multi-disciplinary open access archive for the deposit and dissemination of scientific research documents, whether they are published or not. The documents may come from teaching and research institutions in France or abroad, or from public or private research centers.

L'archive ouverte pluridisciplinaire **HAL**, est destinée au dépôt et à la diffusion de documents scientifiques de niveau recherche, publiés ou non, émanant des établissements d'enseignement et de recherche français ou étrangers, des laboratoires publics ou privés.

Deep Eddy Kinetic Energy in the Tropical Pacific from Lagrangian Floats

A. Delpech¹, S. Cravatte¹, F. Marin¹, C. Ménesguen², Y. Morel¹

¹LEGOS (Laboratoire d'Etudes en Géophysique et Océanographie Spatiales) - Université de Toulouse - CNES - CNRS - IRD, Toulouse, France

²LOPS (Laboratoire d'Océanographie Physique et Spatiale) - Université de Bretagne Occidentale - Ifremer - CNRS - IRD, Brest, France

Key Points:

- Eddy kinetic energy at 1000 m in the tropical Pacific is investigated using Argo float drifts.
- Deep intra-annual variability is evidenced with 30-day period and 1000-km wavelength at the Equator and 70-day, 500-km off the Equator.
- Eddy kinetic energy exhibits small scale features suggesting interactions with the mean jet-like circulation at 1000 m.

Corresponding author: Audrey Delpech, audrey.delpech@legos.obs-mip.fr

Abstract

[At the ocean surface, satellite observations have shown evidence of a large spectrum of waves at low latitudes. However, very little is known about the existence and properties of the deep variability. Most of the subsurface observations rely on localized measurements, which do not allow for a global estimation of this variability. In this study, we use velocity estimates, provided by Argo float drifts at 1000 m, to analyze the spatial and temporal distribution of the deep Eddy Kinetic Energy (EKE) and its spectral signature with an unprecedented time and space coverage. In the tropical Pacific, high EKE is found along the Equator, at the western boundary and poleward of 7°N. EKE meridional distribution is also found to vary at the scale of the meridionally-alternating mean zonal jets: it is higher inside eastward currents. We develop an original statistical scale analysis to determine the temporal and spatial scale-dependence of this deep EKE footprint. We show the presence of periodic features whose characteristics are compatible with theoretical equatorial waves dispersion relations. Annual and semi-annual Rossby waves are observed at the Equator, as well as ~30-day Yanai waves, consistent with surface Tropical Instability Waves. The location and intensification of these waves match the downward energy propagation predicted by ray tracing linear theory. Short-scale variability (with ~70-day periods and 500-km wavelength) has also been detected poleward of 7°N. The generation mechanisms of this variability is discussed, as well as its potential importance for the mean circulation.]

Plain Language Summary

Energy in the deep ocean is important as it is a potential driver of the deep circulation, which has important climate feedbacks. Because of its singular dynamics, the equatorial ocean is a preferential region of transfer of energy from the surface to the interior of the ocean. Very little is known however about the energy content in the deep equatorial oceans. In this study, we use the large number of floats, called Argo floats, drifting at 1000-m depth in the ocean to describe the deep kinetic energy in equatorial regions. We show that various energetic waves are present at 1000 m in the tropical Pacific and we discuss their potential generation mechanisms as well as their implications for the circulation. These new observations may help to validate some theories or numerical simulations of the deep equatorial and tropical circulation.

1 Introduction

The mean circulation at low latitudes is structured into intense eastward and westward flowing currents, called jets. At the surface, currents develop in response to the trade winds, namely the westward North Equatorial Current (NEC) and South Equatorial Current (SEC) (Lagerloef et al., 1999) and the eastward North Equatorial Counter Current (NECC). The eastward Equatorial Undercurrent (EUC) flows inside the thermocline and is confined along the Equator (Wyrтки & Kilonsky, 1984) (see Fig. 1 for a schematic in the Pacific).

Below the thermocline, our knowledge of the circulation is more recent. Thanks to the large number of Argo floats deployed since the beginning of the program in 2000, deep velocity estimates have been made available basin-wide. Several studies have revealed the presence of strong eastward and westward jets, equatorward of 20° (e.g., Ollitrault et al. (2006); Lebedev et al. (2007); Cravatte et al. (2012); Qiu et al. (2013); Ollitrault and Colin de Verdière (2014)) and reaching depths of 2000 m (Cravatte et al., 2017).

The deep zonal velocity has been shown to follow an annual cycle (Cravatte et al., 2012; Zanowski et al., 2019), especially close to the Equator where a reversal of the jets is observed (Gouriou et al., 2006). This has been attributed to the downward propagation of annual Rossby waves (Lukas & Firing, 1985; Marin et al., 2010; Cravatte et al., 2012). At inter-annual timescales, the zonal velocity at 1000 m in the Pacific seems correlated to El Niño fluctuations with 6-month phase lag (Zanowski et al., 2019).

65 Understanding the energy sources and mechanisms at the origin of the deep jets remains
 66 a challenge. Several mechanisms have been proposed (see Ménesguen et al. (2019) for a
 67 review). Although they involve different physical processes, they all require an energy
 68 source in the deep ocean. Based on numerical simulations and theoretical considerations,
 69 several studies have shown that intra-annual waves at depth can provide this energy, driving
 70 a realistic deep circulation (Hua et al., 2008; Ménesguen et al., 2009; Ascani et al., 2010,
 71 2015; Greatbatch et al., 2018; Bastin et al., 2020).

72 The variability in the equatorial regions is strong and has comparable amplitudes with
 73 the mean circulation. Intra-annual variability at depth could result either from a downward
 74 propagation of waves excited in the upper ocean, or could be generated directly at depth
 75 from instabilities of the strongest currents (like the deep western boundary current).

76 At the ocean surface, satellite-derived observations have revealed the presence of a broad
 77 spatial and temporal spectrum of waves at low latitudes (Lindstrom et al., 2014). Among
 78 the most energetic features are the Tropical Instability Waves (TIWs), arising from the shear
 79 between the westward-flowing SEC and the eastward-flowing NECC and EUC (Philander,
 80 1978). They develop along the temperature front at the border of the cold tongue in the
 81 eastern part of the basin (Fig. 1) from July to November, when the temperature gradient
 82 is the highest (see Willett et al., 2006, for a review). They have been observed both in
 83 the Atlantic and Pacific oceans from satellite altimetry (Legeckis, 1977; Lyman et al., 2005,
 84 2007; Farrar, 2011; Lindstrom et al., 2014, and references therein), but also in in-situ
 85 meridional velocities (McPhaden, 1996; Lyman et al., 2007) and temperatures (McPhaden,
 86 1996; Chelton et al., 2000; Contreras, 2002). In the Pacific, they have a signature at the
 87 Equator and 5°N associated with periods of 17 and 30 days respectively (Lyman et al.,
 88 2007).

89 However, observational evidence of deep intra-annual variability remains scarce. Most
 90 of the observations rely on sparse mooring measurements or cruise transects. Equatorial
 91 moorings data have evidenced a strong signature in meridional velocity at 30-50 days periods
 92 in the upper 600 m (Von Schuckmann et al., 2008, in the Atlantic) and in the range 20-90
 93 days in the Pacific (Wang et al., 2016; Zhang et al., 2020). Deeper observations down to 3000
 94 m (e.g., Bunge et al. (2008); Tuchen et al. (2018) in the Atlantic, Eriksen and Richman (1988)
 95 in the Pacific) also revealed the presence of intra-annual variability. This variability has been
 96 related to the downward propagation of mixed Rossby-Gravity waves possibly generated
 97 by TIWs (Tuchen et al., 2018). In addition, in the Equatorial Pacific ocean, Farrar and
 98 Durland (2012) have noted the presence of variability of surface dynamic height relative to
 99 500 dbars, in the period range 5-15 days associated with Inertia-Gravity and mixed Rossby-
 100 Gravity waves. Along the western boundary in the Equatorial Pacific, deep intra-annual
 101 variability has been attributed to the signature of strong subthermocline mesoscale eddies
 102 (Firing et al., 2005). However, the information provided by the moorings or cruise transects
 103 is very incomplete. It only gives a local estimate of the period or wavelength and does not
 104 allow for full characterisation of scales. A global and more systematic assessment of this
 105 deep variability is still lacking.

106 In this study, we assess the variability in the deep tropical Pacific, with a focus on
 107 intra-annual periods. We aim to characterise its spectral range (both temporal and spatial)
 108 and variations at the basin scale. We will in particular address the following questions:
 109 (1) What are the amplitudes and characteristic (temporal and spatial) scales of the energy
 110 present at depth in the tropical Pacific ? (2) Is there a spatial and temporal modulation of
 111 the observed signals ? (3) Is there coherence of the signals that could be related to particular
 112 physical processes, such as wave or eddy propagation ?

113 We address these questions by analyzing the fluctuations of the 10-day averaged La-
 114 grangian velocity measured by the Argo float displacements at 1000 m in the tropical Pacific.
 115 We develop statistical methods of scale analysis that extract information from these numer-
 116 ous and sparse velocity estimates. The relationship between the velocities measured at the

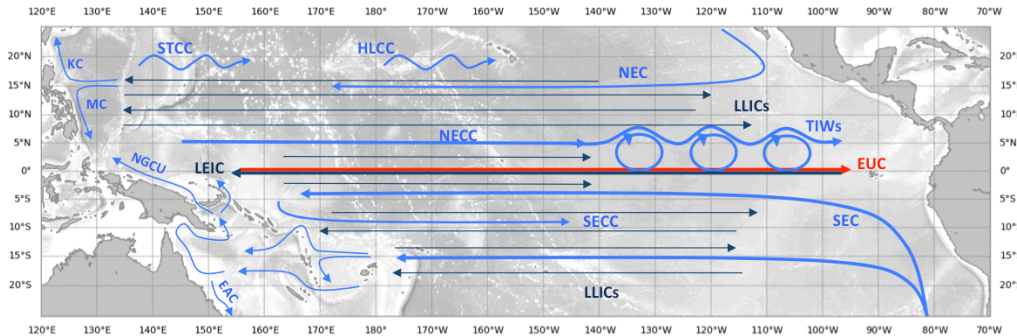


Figure 1. Schematics of the Pacific ocean circulation. Light blue: surface currents, red: thermocline currents, deep blue: deep currents. NEC: North Equatorial Current, SEC: South Equatorial Current, NECC: North Equatorial Counter Current, SECC: South Equatorial Counter Current, HLCC: Hawaiian Lee Counter Current, STCC: Subtropical Counter Current, TIWs: Tropical Instability Waves, EUC: Equatorial Undercurrent, LEIC: Lower Equatorial Intermediate Current, LLICs: Low-Latitude Intermediate Currents. Reproduced after Smith et al. (2019).

117 same time between pairs of floats gives insight into the spatial scales of the dynamical structures.
 118 Similarly, the relationship between sequential measurements gives information on the
 119 temporal scales of these structures. In addition, combined spatial and temporal dependence
 120 can give information on the propagation of the signals. To be valid, a statistical analysis
 121 requires a critical number of data. This was made possible by the increasing number of
 122 Argo floats since the beginning of the program (Fig. 2), and in particular by the seeding
 123 of hundreds of floats in the Equatorial Pacific in 2014 (Roemmich et al., 2019). Given the
 124 temporal data sampling of the Argo program, this study focuses on periods from 20 days to
 125 annual.

126 The paper is organized as follows: Section 2 describes the data set and the statistical
 127 methods. Section 3 describes the spatial and temporal variations of the eddy kinetic energy
 128 in the tropical Pacific and identifies some energetic regions. Then, in each identified region,
 129 the scale dependence of the energy content is analyzed. Section 4 discusses these results
 130 in the light of processes associated with propagating Equatorial waves and their potential
 131 implication for the regional dynamics. Some limitations of our study are also identified
 132 along with suggestions for future research.

133 2 Data and Method

134 2.1 Database description

135 The data used in this study are the deep velocity estimates from the displacements
 136 of Argo floats at their parking depth. These velocities are computed from the float drifts
 137 along their trajectories, estimated from the floats differential surface positions fixed by
 138 satellite between each dive cycle. These estimates result in a series of nearly 10-day averaged
 139 Lagrangian deep velocities. These estimates include horizontal velocities measured when
 140 profiling from 0-2000 m and back (about a half-day out of every 10 day cycle). This source
 141 of uncertainty is usually small (around 0.4 cm s^{-1} in the Tropical Pacific, see Cravatte et
 142 al. (2012) and Ollitrault and Rannou (2013)) and can be neglected on average.

143 We denote N the total number of velocity estimates, N_i , the total number of ve-
 144 locity estimates for the float i (corresponding to the number of dive cycles for the float
 145 i) and M the total number of floats, such that $\sum_{i=1}^M N_i = N$. For a given float i , we

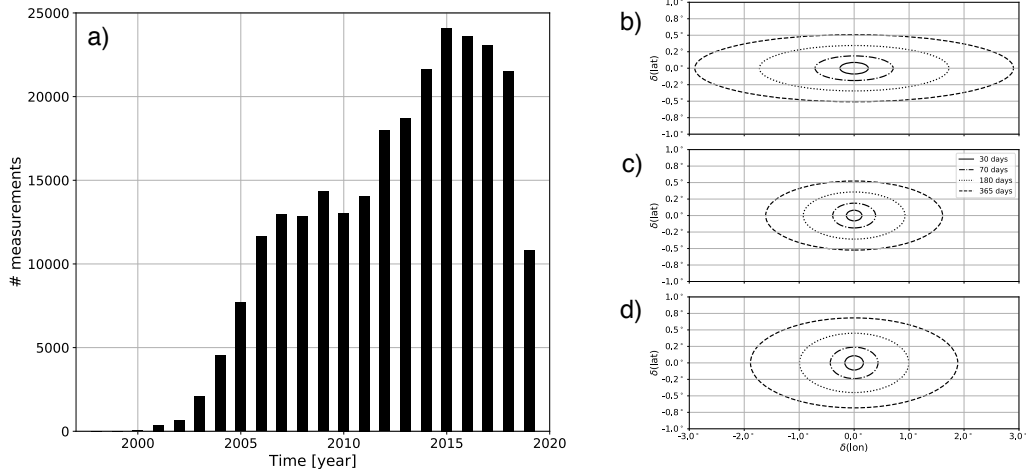


Figure 2. YoMaHA database statistics. (a) Number of 1000 m velocity measurements per year in the tropical Pacific (update through August 2019). The 2014–2018 period corresponds to the most sampled period with a density exceeding 20000 measurements per year. (b–d) Mean displacement $\delta(\text{lon})$, $\delta(\text{lat})$ of floats over different periods (30, 70, 180 and 365 days) in the different regions: (b) Equatorial Pacific (west and east) 165°E – 90°W , 3°S – 3°N , (c) Tropical Pacific (north and south), 170°E – 90°W , 7° – 17° S and N and (d) western boundary 125°E – 135°W , 0° – 17°N .

146 denote zonal and meridional velocities series respectively as $(U_n^i(x_n^i, y_n^i, t_n^i))_{n \in \{1..N_i\}}$ and
 147 $(V_n^i(x_n^i, y_n^i, t_n^i))_{n \in \{1..N_i\}}$, where x_n^i , y_n^i and t_n^i are the mean longitude, latitude and time for
 148 the dive cycle n .

149 The deep velocity estimates used are provided by the YoMaHA database updated
 150 through August 2019 (Lebedev et al., 2007). Although similar databases exist with per-
 151 haps more accurate velocity estimates (e.g., ANDRO from Ollitrault and Rannou (2013)),
 152 the YoMaHA database has been preferred in this study because it is nearly real-time up-
 153 dated and provides the densest coverage in our region of interest. The majority of the
 154 floats (63%) are programmed for a 1000 m parking depth. In the remainder of this paper,
 155 we perform our diagnostics on the 1000 m velocity estimates only by keeping floats whose
 156 parking depth is between 950 m and 1050 m. The other depths do not provide a sufficient
 157 coverage for a statistical approach and are discarded. Speeds in excess of 40 cm s^{-1} , found
 158 in 0.07% of the samples, were rejected as outliers. Some statistics about the number of floats
 159 and measurements of this dataset available in the tropical Pacific, as well as the different
 160 regions considered in this study (Section 3), are presented in Table 1 and Fig. 2.

161 In the following, we consider either timeseries of velocity for each float i : $(U^i(t_n^i))_{n \in \{1..N_i\}}$, $(V^i(t_n^i))_{n \in \{1..N_i\}}$
 162 (Section 2.2.2), or series of independent velocity estimates, regardless of the float number:
 163 $(U_n, V_n)_{n \in \{1..N\}}$ (Section 2.2.3).

164 2.2 Method

165 2.2.1 Energy variables definition

166 As the aim of this study is to characterize the deep variability, we perform a classical
 167 Reynolds decomposition of the velocity to separate the mean and the variable part of the
 168 flow:

$$\begin{cases} U(x, y, t) = \bar{U}(x, y) + U'(x, y, t) \\ V(x, y, t) = \bar{V}(x, y) + V'(x, y, t) \end{cases} \quad (1)$$

169 where the overbar indicates the time average for the whole period 1997-2019 and the prime
170 the fluctuations with respect to this average.

171 We define the Mean Kinetic Energy (MKE) and Eddy Kinetic Energy (EKE) at any
172 given location x, y as twice the kinetic energy per unit mass contributed by their respective
173 velocity components:

$$\begin{aligned} \text{MKE}_q(x, y) &= \overline{q(x, y, t)^2} = \bar{q}(x, y)^2 \\ \text{EKE}_q(x, y) &= \overline{q'(x, y, t)^2} \\ &= \overline{(q(x, y, t) - \bar{q}(x, y))^2} \end{aligned} \quad (2)$$

174 where $q = (U_n)_{n \in \{1..N\}}$ or $q = (V_n)_{n \in \{1..N\}}$.

175 Previous studies have shown that the annual cycle is the dominant mode of variability
176 of the 1000 m zonal currents in the equatorial region (Cravatte et al., 2012). In order
177 to estimate the other periods of variability, we define U^* as the zonal velocity where the
178 monthly climatology has been filtered out.

$$U^*(x, y, t) = U(x, y, t) - U^m(x, y, t) \quad (3)$$

179 where the superscript m refers to the monthly climatology of U . The associated eddy kinetic
180 energy is:

$$\text{EKE}_U^*(x, y) = \overline{U^*(x, y, t)^2} \quad (4)$$

181 EKE_U^* contains thus both the intra-annual and inter-annual components of the zonal velocity
182 fluctuations.

183 In practice, $(U_n)_{n \in \{1..N\}}$ and $(V_n)_{n \in \{1..N\}}$ are unstructured fields: position and time
184 change for each measurement, and there are no repeated measurements at any location.
185 The time-averaged fields \bar{U} , \bar{V} and U^m are thus obtained from a gridding method. Here we
186 use optimal interpolation of the fields from Cravatte et al. (2012). The EKE field is then
187 computed from a simple binned-average with a bin size of $1^\circ \times 1^\circ$.

188 Following Roulet et al. (2014), we define the Eddy Available Potential Energy (EAPE)
189 as:

$$\text{EAPE}(x, y) = -\frac{g}{2\rho_0} \overline{\zeta'(x, y)\rho'(x, y)} \quad (5)$$

190 where ζ' is the vertical isopycnal displacement and ρ' the density anomaly associated with
191 this displacement. The EAPE used in this study comes from the dataset (Roulet, 2020).
192 The EAPE has been computed for each Argo profile (0-2000 m) at 63 vertical levels and
193 binned on a $0.25^\circ \times 0.25^\circ$ horizontal grid. In this study we extracted the 1000 m-level.
194 Outliers exceeding one standard deviation have been discarded. This corresponds to 1.3%
195 of the data.

196 **2.2.2 Estimation of dominant periods of variability from wavelet transform**

197 The dominant period is computed from the deep velocity time series associated with
198 each individual float trajectory (e.g., Fig. 3a-c). A continuous wavelet transform using a
199 complex Morlet wavelet with periods from 10 to 450 days and a 1-day increment is performed
200 on these time series (Lee et al., 2019). This method results in a local estimation of the

201 amplitude of the signal at each frequency (Fig. 3d). Note that it is not possible to estimate
 202 the wavelet transform for all periods near the beginning or the end of the time series,
 203 where edge effects potentially contaminate the signal (Torrence & Compo, 1998). Periods
 204 within this cone of influence are not considered (Fig. 3d). For each measurement time (or
 205 equivalently position), the period with the largest amplitude, A_n , is selected as the dominant
 206 period P_n . Amplitude weighted histograms of dominant periods, H_Ω , are then constructed
 207 in a given region Ω of the (x, y) plane, following Eq. 6:

$$H_\Omega(p, p + dp) = \frac{1}{N_\Omega} \left(\sum_{n \mid \substack{(x_n, y_n) \in \Omega \\ p < P_n < p + dp}} A_n \right) \quad (6)$$

208 where p is a given period and dp an increment. Here, we use p going from 10 to 450 days,
 209 with $dp = 10$ days. N_Ω is the total number of measurements in the region of consideration.
 210 Note that this method retains only the most energetic frequency, regardless of the energy
 211 present at other frequencies.

212 Four approximations are made for the computation of the dominant period:

213 First, we consider the velocity from the float time series as a real time series made
 214 of instantaneous velocities, while the velocity estimates given by the Argo product are \sim
 215 10-day averaged Lagrangian velocities along float trajectories. This will filter out signals
 216 with periods shorter than 10 days. In addition, the time series has a 10-day sampling rate
 217 following the Argo cycle. The corresponding Nyquist frequency is one cycle per 20 days.
 218 Aliasing of higher frequencies is reduced but not eliminated by the 10-day averaging.

219 Second, we neglect the Lagrangian character of the measurements and take the velocity
 220 time series as an Eulerian time series. This assumption is valid as long as the distance
 221 travelled by the float during the estimated wave period is short with respect to the wave-
 222 lengths of the waves. The mean displacement of the floats increases with the estimated
 223 period, and is maximal in the equatorial regions (Fig. 2b-d). It reaches 1.5° longitude and
 224 0.5° latitude at intra-annual periods (typically 70 days) and 6° longitude and 1° latitude
 225 at annual periods. The zonal displacements are short compared to the wavelengths derived
 226 from the Equatorial waves dispersion relations ranging from a few hundreds of kilometers at
 227 intra-annual periods to thousands of kilometers at annual periods. Likewise, the meridional
 228 displacements remain shorter than the equivalent meridional wavelength of the Equatorial
 229 waves (which are trapped within a few degrees of the Equator).

230 Third, we neglect the Doppler shift. In presence of a mean flow, the apparent period of
 231 the wave is indeed modified (e.g., Barbot et al. (2018)). This effect is stronger as the mean
 232 flow approaches the phase speed of the wave (see Appendix A).

233 Fourth, we neglect the Stokes drift, a non-linear advection of a particle in a wave
 234 motion, directed along the phase speed of the wave. It is generally weak (Weber, 2017) and
 235 is assumed to be negligible with respect to the mean currents.

236 As shown in the next sections, these approximations are validated *a posteriori* by the
 237 consistency of our results with other diagnostics.

238 **2.2.3 Statistical Scale Analysis**

239 One of the aims of this study is to determine the scale dependence associated with
 240 the deep EKE footprint. Classical spectral analyses, including Fourier transforms, generally
 241 require uniformly sampled data. This condition is difficult to achieve with in-situ observa-
 242 tions unless applying interpolation pre-processing. Moreover such methods can introduce
 243 significant errors, in particular when data are scarce. We thus develop in this study a met-

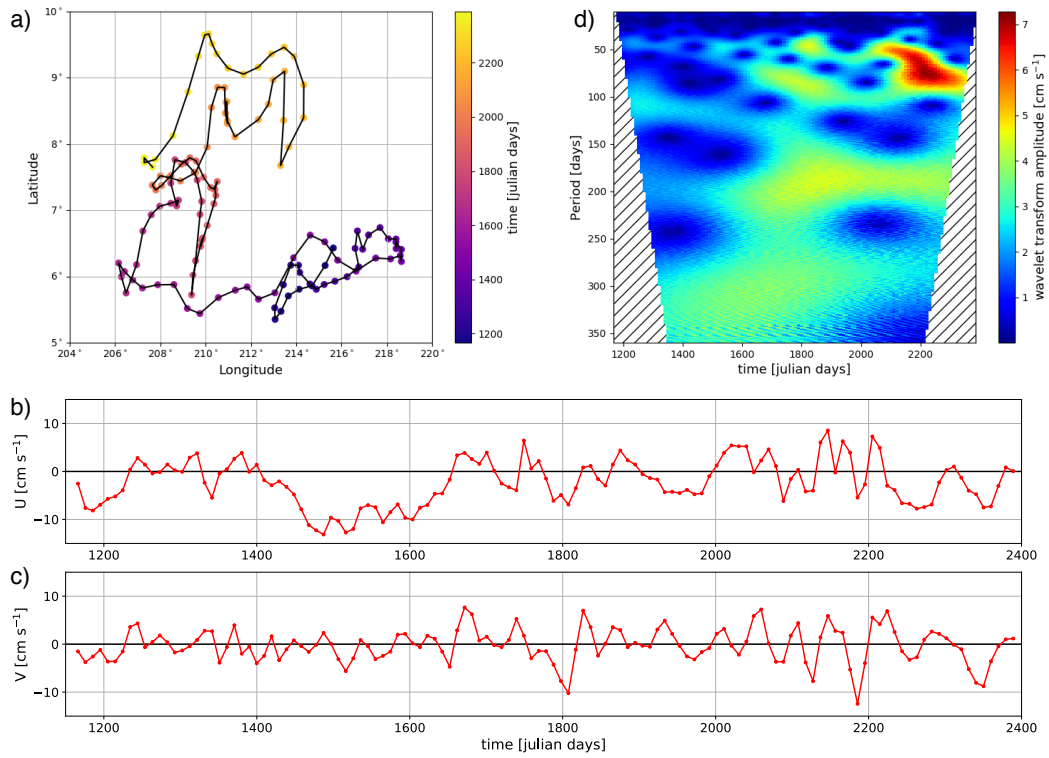


Figure 3. (a) Example of an individual float trajectory as a function of time (colorscale) from the YoMaHA database (float n°3557) (b) float U time series, (c) float V time series, (d) wavelet analysis of the V time series. The dashed area indicates the cone of influence; in this area, the estimations are biased by edge effects and are thus not considered.

244 ric that measures both the spatial and temporal scale dependence of the horizontal velocity
 245 anomalies from the unstructured Argo measurements.

246 This metric has been largely inspired by structure functions (Babiano et al., 1985;
 247 Sérazin et al., 2020), developed to compute the scale dependence of kinetic energy from
 248 irregular data sampling (Morel & Larcheveque, 1974). They have been successfully applied
 249 to Lagrangian float measurements to study turbulent energy cascades (McCaffrey et al.,
 250 2015; Balwada et al., 2016). Most of the studies using structure functions however assume
 251 homogeneous, stationary and isotropic flow statistics. These assumptions seem reasonable
 252 for mid-latitude fully developed turbulence regimes but not for low-latitude wave-dominated
 253 regimes.

254 We define the Statistical Scale Function (hereafter SSF) as the mean squared difference
 255 between quantities at points separated by a given distance and time lapse. Because it
 256 considers both space direction and time separations, SSF accounts for the anisotropy of
 257 the flow and captures propagating patterns. It still assumes a statistical stationarity (the
 258 spectral characteristics of the variability do not evolve in time).

259 Denoting δq the increment of a quantity q between two independent measurements (i, j)
 260 with positions \vec{x}_i and \vec{x}_j and time t_i and t_j :

$$\delta q(\vec{x}_i, t_i, \vec{x}_j, t_j) = q(\vec{x}_j, t_j) - q(\vec{x}_i, t_i). \quad (7)$$

261 Under the assumption of homogeneity (the statistics do not depend on space and time in
 262 the region of focus), we define the SSF D_q , of a quantity q as:

$$D_q(\vec{dx}, dt) = \frac{1}{n_{ij}} \sum_{\substack{\{i,j\} \\ \vec{x}_j - \vec{x}_i = \vec{dx} \\ t_j - t_i = dt}} \delta q(\vec{x}_i, t_i, \vec{x}_j, t_j)^2 \quad (8)$$

263 where \vec{dx} and dt are given separation vector and time lapse, $\{i, j\}$ are the possible pairs of
 264 measurements that satisfy the condition $\vec{x}_j = \vec{x}_i + \vec{dx}$ and $t_j = t_i + dt$, with n_{ij} the number
 265 of such pairs. $D_q(\vec{dx}, dt = 0)$ corresponds exactly to the second order structure function of
 266 the quantity q .

267 Here, q is taken as U, V for the zonal and meridional components of the velocity.
 268 In addition, we generally only take into account the zonal component of the separation
 269 scale ($\vec{dx} = dx \vec{i}$) as we mostly expect zonal propagation, and will simply write $D_q(dx, dt)$.
 270 Taking the full separation vector ($\vec{dx} = dx \vec{i} + dy \vec{j}$) would considerably reduce the number
 271 of pairs available at a given separation scale and would not lead to robust statistics. As a
 272 consequence, computing SSF assumes homogeneous variables along the meridional direction.
 273 For this assumption to be valid, we apply this metric in regions where we expect homogeneity
 274 (Section 3.3). Tests have shown that our results are not particularly sensitive to the borders
 275 of the regions within which we calculate SSF.

276 The separation scales, dx, dt , of the increments are binned on a $0.5^\circ \times 5$ days grid,
 277 yielding at least 100 pairs by bin. The size of the bins used for the gridding directly
 278 determines the scales that are resolved for dx and dt . Assuming that the effective resolution
 279 is approximately 3 times the grid resolution, the chosen grid resolves scales $dx > 1.5^\circ$ and
 280 $dt > 15$ days. Given the time series length and the region dimensions, periods longer than
 281 9 years and zonal wavelengths shorter than 160° are filtered out. In order to avoid large
 282 noise, only scales (dx, dt) for which the number of measurements is greater than 100 are
 283 considered.

284 As an example, we consider the ideal case of a velocity field corresponding to a plane
 285 wave propagating along the x-direction. The wave is associated with the following velocity
 286 field:

$$\begin{cases} u(x, t) = 0 \\ v(x, t) = v_0 \sin(k_0 x - \omega_0 t) \end{cases} \quad (9)$$

287 It can be shown that the SSF is equal to zero along the phase line of the wave. Denoting
288 c_0 the phase speed of the wave ($c_0 = \frac{\omega_0}{k_0}$), the phase lines are defined by the equation
289 $dx = c_0 dt$, and:

$$D_v(c_0 dt, dt) = \frac{1}{n_i} \sum_i [v_0 \sin(k_0 x_i - \omega_0 t_i) - v_0 \sin(k_0(x_i + \frac{\omega_0}{k_0} dt) - \omega_0(t_i + dt))]^2 = 0 \quad (10)$$

290 In particular, the SSF is equal to zero when the separation distance is equal to the wavelength
291 and $dt = 0$ or when the time difference is equal to the period of the wave and $dx = 0$:

$$\begin{cases} D_v(0, \frac{2\pi}{\omega_0}) = 0 \\ D_v(\frac{2\pi}{k_0}, 0) = 0 \end{cases} \quad (11)$$

292 The amplitude of the wave can be estimated from the amplitude of the SSF along its maximal
293 amplitude lines (where either the distance is equal to the half wavelength or the time lapse
294 is equal to the half period of the wave):

$$D_v(\frac{2\pi}{2k_0}, 0) = \frac{1}{n_i} \sum_i [v_0 \sin(k_0 x_i - \omega_0 t_i) - v_0 \sin(k_0(x_i + \frac{2\pi}{2k_0} dt) - \omega_0 t_i)]^2 \quad (12)$$

$$= 4v_0^2 \frac{1}{n_i} \sum_i \sin^2(k_0 x_i - \omega_0 t_i) = 2v_0^2 \quad (13)$$

295 assuming that (x, t) is uniformly randomly sampled and therefore that $\frac{1}{n_i} \sum_i \sin^2(k_0 x_i - \omega_0 t_i) = \frac{1}{2}$.
296

297 In practice, the velocity is unlikely to be a pure wave field and velocities available
298 from the Argo dataset are not instantaneous Eulerian velocities but averaged Lagrangian
299 velocities. So we do not expect the SSF to be equal to zero at the scales corresponding to the
300 wavelength and wave period, but rather to reach a minimum, and we expect the amplitude
301 of the SSF to be underestimated. Similarly, if (x, t) is not uniformly sampled, the SSF at the
302 half-period and half-wavelength may depart from the theoretical formula given in Eq. 13.
303 In addition the waves might be dissipated, or wavetrains with different phases might coexist
304 and will reduce the coherence of the SSF signal at large dx and dt . The signature of the
305 dominant wave, if any, will thus more likely stand out for space time separation within a
306 few wavelengths or periods near the origin ($dx = 0, dt = 0$).

307 This method has been validated by advecting synthetic floats within a prescribed wave
308 field and by controlling that the estimated wavelength and period match the prescribed
309 ones (see Appendix B). Fig. B1 gives the typical SSF pattern if a wave signal dominates the
310 dynamics. Given the limits of the method discussed above, we expect the amplitude to be
311 generally underestimated. There are however fewer approximations with this method than
312 with wavelet transforms described in Section 2.2.2.

313 **3 Results**

314 **3.1 Deep Eddy Kinetic Energy (EKE) in the tropical Pacific**

315 **3.1.1 Inhomogeneity of the spatial distribution of EKE**

316 The deep (1000 m) zonal EKE (EKE_U) is spatially inhomogeneous. It is larger at
317 the Equator, especially in the 170°E-160°W longitude range where it can reach up to 200

318 cm^2s^{-2} (Fig. 4a and 5a). Part of this signal can be attributed to the annual variability,
 319 which is strong at the Equator and decreases poleward to 8° (Cravatte et al., 2012). Once
 320 the mean annual cycle is filtered out, the residual EKE (EKE_{U^*}) containing the intra- and
 321 inter-annual variability still shows a maximum along the Equator, although its amplitude
 322 is reduced to $170 \text{ cm}^2\text{s}^{-2}$, and the western part (170°E - 160°W) of the signal has been
 323 considerably reduced (Fig. 4b). A second relative EKE_U maximum ($\sim 40 \text{ cm}^2\text{s}^{-2}$) also shows
 324 up north of the Equator (10°N - 17°N), while the southern hemisphere ($< 5^\circ\text{S}$) exhibits a
 325 very weak EKE_U ($< 10 \text{ cm}^2\text{s}^{-2}$).

326 The deep (1000m) meridional EKE (EKE_V) also has an heterogeneous regional distribu-
 327 tion. The dominant signal ($> 100 \text{ cm}^2\text{s}^{-2}$) is found along the western boundary (Fig. 4c).
 328 The EKE_V is also larger at the Equator, with distinct maxima in the western part ($\sim 170^\circ\text{E}$ -
 329 170°W) and in the eastern part ($\sim 130^\circ\text{W}$ - 110°W) of the basin (Fig. 4c). A relatively large
 330 amount ($\sim 30 \text{ cm}^2\text{s}^{-2}$) of EKE_V is also found in the northern part of the basin (10°N - 17°N)
 331 (Fig. 4c and 5b), while the EKE_V in the southern hemisphere is concentrated around the
 332 many islands, west of 170°W (Fig. 4c).

333 Superimposed on this large regional scale distribution of zonal and meridional EKE,
 334 variations of the amplitude are also observed at small meridional scales (Fig. 5a and 5b),
 335 with zonally-coherent, meridionally-alternating maxima and minima of EKE. When com-
 336 pared to the structure of the meridionally-alternating mean zonal velocities (Cravatte et al.
 337 (2012), blue curve Fig. 5), local EKE maxima are found to coincide with eastward jets and
 338 local EKE minima with westward jets equatorward of 15° . EKE_U local maxima are also
 339 observed in westward jets at 4°S and 7°S though.

340 Based on these results, we define 5 regions in which we analyze the characteristics of the
 341 large-scale EKE distribution in the following sections 3.2 and 3.3: the Eastern Equatorial
 342 region (EE: 155°W - 90°W , 3°S - 3°N), the Western Equatorial region (EW: 165°E - 175°W ,
 343 3°S - 3°N), the North Tropical Pacific (TN: 170°E - 125°W , 7°N - 17°N), the South Tropical
 344 Pacific (TS: 160°W - 90°W , 7°S - 17°S) and the Western Boundary region (WB: 125°E - 135°E ,
 345 0° - 17°N) (Fig. 4c). The small-scale (jet-scale) EKE distribution is investigated in Section 3.4.

346 **3.1.2 Annual modulation of the EKE**

347 A monthly climatology of the EKE shows that some regions undergo an annual intensi-
 348 fication of the EKE. This is the case in particular in EE region, where stronger EKE_V (up
 349 to $35 \text{ cm}^2 \text{ s}^{-2}$) is observed in boreal autumn and winter (September to February) (Fig. 6a).
 350 Similarly in the TN region, EKE_V increases from 10 to $15 \text{ cm}^2 \text{ s}^{-2}$ between June and De-
 351 cember. Although it is less pronounced, the EW region also follows the same annual cycle,
 352 with an increase of EKE_V from 15 to 17 - $20 \text{ cm}^2 \text{ s}^{-2}$ between May and December-January.
 353 The EKE_U at the Equator also present annual intensification mostly during spring and
 354 summer times (Fig. 6b). In the EW region, EKE_U increases to $225 \text{ cm}^2 \text{ s}^{-2}$ between June
 355 and September. In the EE region, EKE_U is intensified (up to $120 \text{ cm}^2 \text{ s}^{-2}$) between May
 356 and August (Fig. 6b). Conversely, TS and WB regions do not present any climatological
 357 annual variations.

358 **3.2 Dominant Periods of Variability**

359 This section investigates the temporal scales (periods) associated with the velocity
 360 anomalies (U' , V' and U^*) in the different regions identified in section 3.1. Figure 7 shows
 361 the dominant periods in the different regions from the amplitude weighted histograms, as
 362 described in Section 2.2.2.

363 The zonal velocity U' is mostly associated with long periods (> 150 days). The Equator-
 364 torial region (EW and EE) shows a dominant annual period of ~ 360 days, that can be
 365 associated with the well-documented vertically-propagating annual Rossby wave (Fig. 7b)
 366 (Kessler & McCreary, 1993; Marin et al., 2010). In addition the EE region has energy at

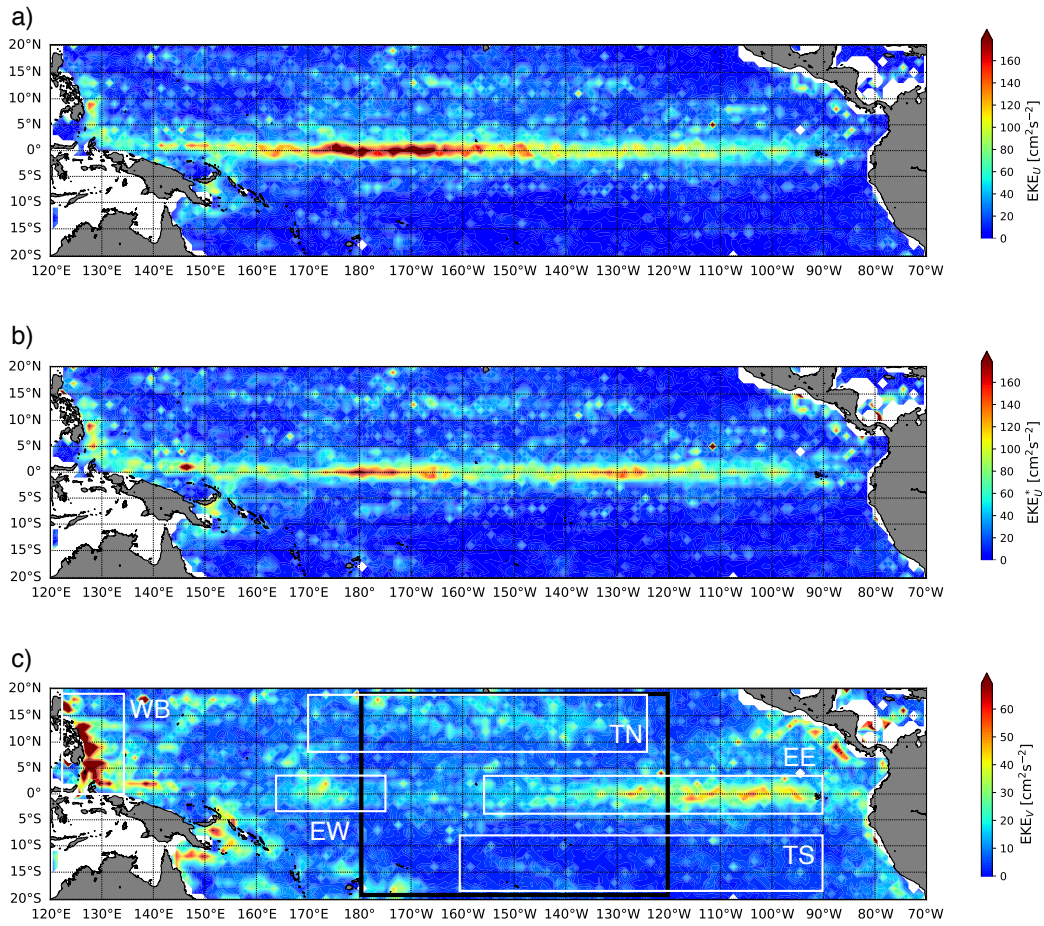


Figure 4. Map of (a) EKE_U , (b) EKE_U^* (corresponding to the EKE associated with the zonal component of the velocity for which the mean annual cycle has been filtered out), (c) EKE_V computed from the 1000m velocity anomalies and binned on a $1^\circ \times 1^\circ$ horizontal grid over the period 1997-2019.

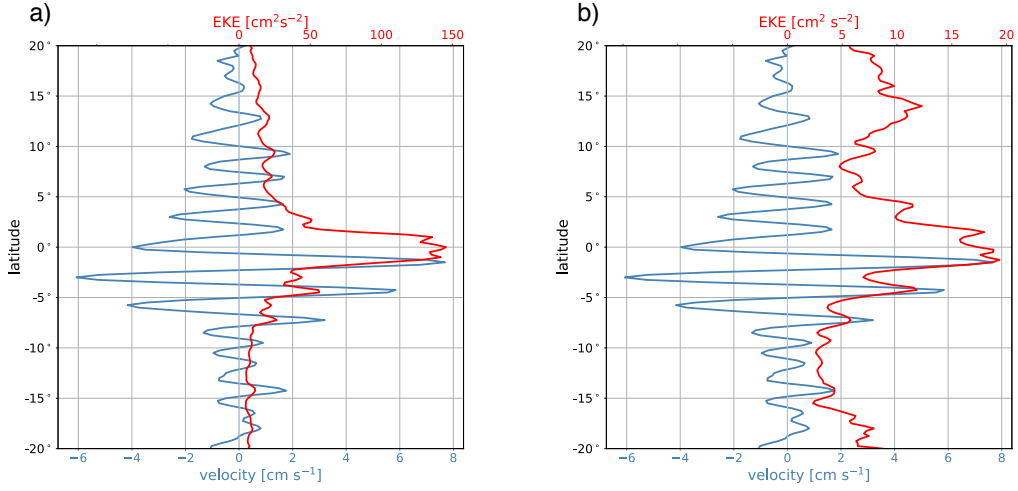


Figure 5. Mean zonal velocity $\bar{U}(y)$ (blue) and (a) EKE_U , (b) EKE_V (red) at 1000 m averaged from 180° to 120° W (black box shown in Fig. 4) over the period 1997-2019.

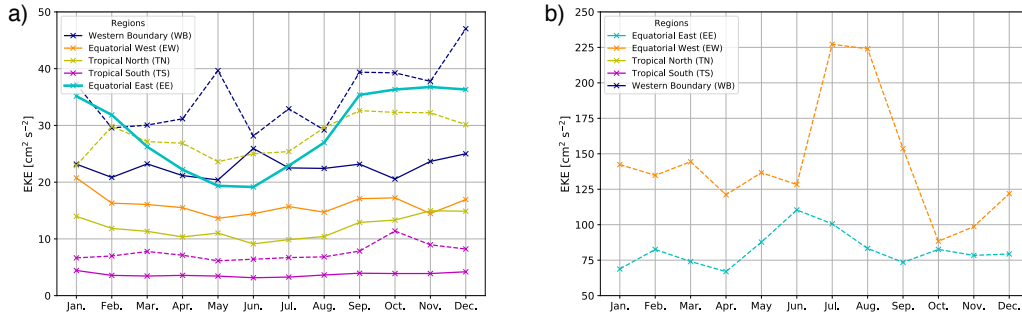


Figure 6. Monthly climatology (average from the first day to the last day of each month) of the EKE_U (dashed) and EKE_V (solid) in the different regions (colors) zoomed between (a) 0-50 cm^2s^{-2} and (b) 50-250 cm^2s^{-2} .

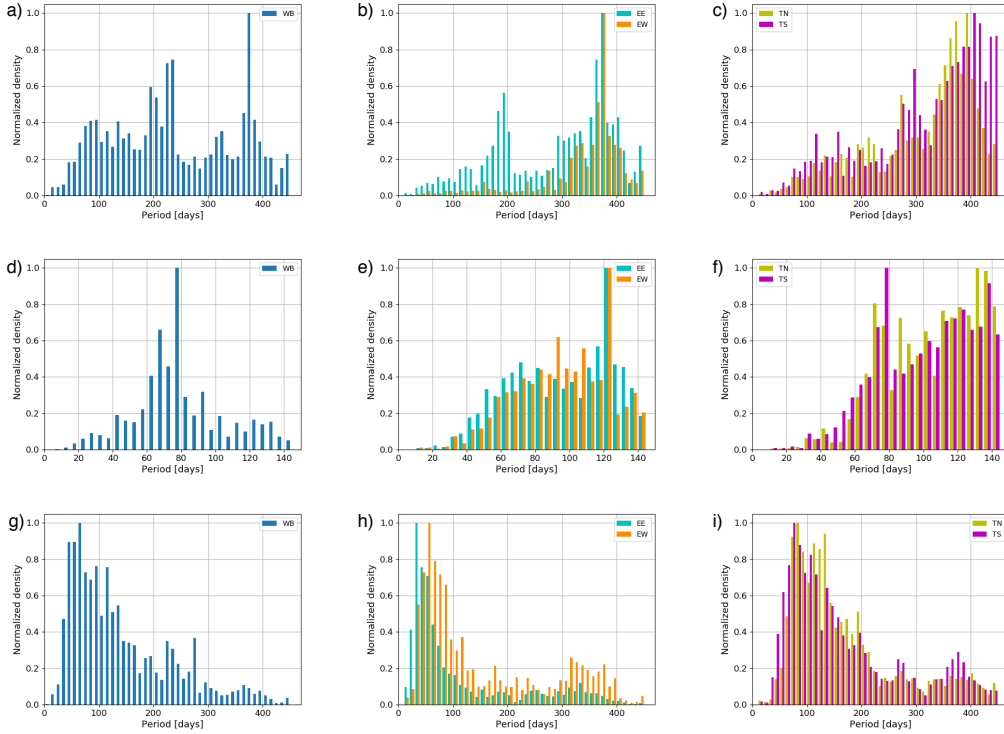


Figure 7. Periodograms for U' (top), U^* (middle) and V' (bottom) at the western boundary (left), in the equatorial regions (middle) and in the extra-equatorial regions (right). The periodograms are computed from wavelet analysis as $\frac{H}{H_{max}}$, where H follows Eq. 6. It is computed for periods from 10 to 450 days with 10-day increments for U' and V' and from 10 to 145 days with 5-day increments for U^* .

367 semi-annual period. Off-Equatorial regions (TN and TS) have peak energy amplitude in the
 368 350-380 period range (Fig. 7c). When filtering out the mean annual cycle (U^*) and focusing
 369 on the intra-annual variability, a dominant period of 120 days is found at the Equator
 370 (Fig. 7e) and an energy peak is found in the period range 60-80 days in the WB region and
 371 around 75 days in TN and TS regions (Fig. 7d and 7f respectively).

372 Conversely, the meridional velocity V' is dominated by intra-annual periods (< 150
 373 days) in all regions. Dominant periods of 30 days are found in the EE region (Fig. 7h),
 374 50-day periods in the WB and EW regions (Fig. 7g and 7h) and ~ 75 -day periods in the TN
 375 and TS regions (Fig. 7i).

376 As explained in Section 2.2.2, this method retains the dominant period, but variability
 377 at other periods may be present too. In particular, this could explain why maxima of U'
 378 and V' variability are not found in the same period ranges. The two variables are the
 379 dominant signature of different variability sources. It is however interesting to notice the
 380 similarity between U^* and V' . Both variables have intra-annual variations with a dominant
 381 period around 75 days off the Equator.

382 3.3 Regional Statistical Scale Analysis

383 Hovmöller diagrams of the zonal and meridional velocity anomalies estimated from
 384 individual floats along given latitudes (eg., along the Equator in Fig. 8) show an organisa-

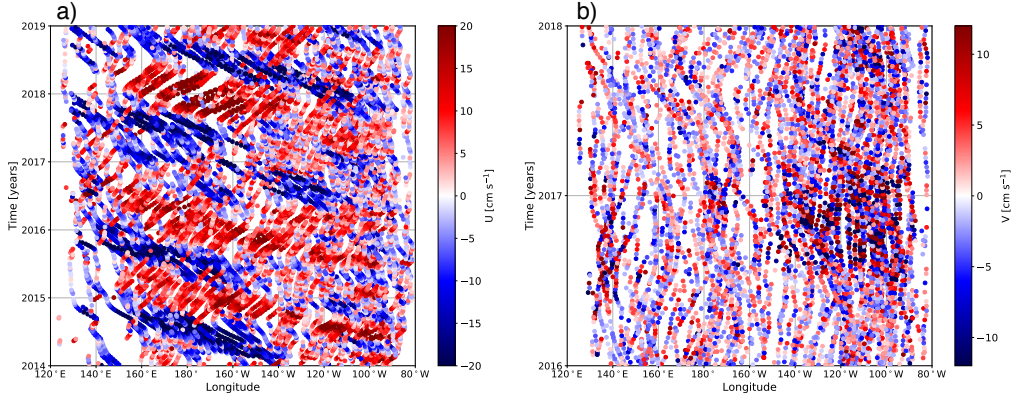


Figure 8. Hovmöller diagram of (a) zonal (U) and (b) meridional (V) 1000 m velocities along the Equator, within the latitude range 2°S - 2°N .

385 tion of the positive and negative anomalies of the velocity into tilted lines, consistent with
 386 westward propagation of waves or eddies

387 The period and wavelength can be estimated as the interval between two anomalies
 388 of the same sign on the Y-axis and X-axis respectively. The zonal velocity is associated
 389 with longer periods and wavelengths (around 1 year and several thousands of km) (Fig. 8a)
 390 than the meridional velocity (few days and few degrees) (Fig. 8b). In addition, zonal and
 391 meridional velocities do not share constant periods, wavelengths and amplitudes across the
 392 basin. The zonal velocity has longer periods (~ 1 year) in the western part (west of 220°)
 393 than in the eastern part of the basin (\sim half a year east of 220°E) (Fig. 8a). The meridional
 394 velocity shows a clearer pattern of phase lines east of 180° , where the amplitude of the
 395 velocity is also larger ($>10 \text{ cm s}^{-1}$).

396 Although the Hovmöller diagram already determines the period and wavelength asso-
 397 ciated with the observed anomalies, it presents some limitations. First, it requires a large
 398 number of measurements concentrated in some longitude-time intervals. This requirement
 399 is met only in certain regions such as the eastern Equatorial Pacific. Second, the short scales
 400 are difficult to capture with this method (e.g., Fig. 8b).

401 These reasons led us to develop the statistical scale analysis approach presented in
 402 Section 2.2.3. This approach no longer considers the time and position of each observation
 403 but rather the time difference and the distance between pairs of observations. This takes
 404 better advantage of all available information, leading to a more robust estimation. In the
 405 remainder of this section, the temporal and spatial characteristics of the velocity components
 406 are investigated in each region defined in Table 1 and Fig. 4c using the SSF described in
 407 Section 2.2.3.

408 **3.3.1 Western Equatorial Pacific (EW)**

409 The $\text{SSF}_{U'}$ in the EW region shows three relative minima and two relative maxima
 410 along tilted lines (Fig. 9a). A minimal amplitude of the SSF is associated with a maximal
 411 phase correlation with respect to the origin. The time lapse dt and distance dx at which
 412 SSF is minimal are multiples of the period and wavelength (Section 2.2.3). The period can
 413 be easily estimated by finding where minimal lines cross the $dx = 0$ axis. This is found
 414 for $dt = 0$, $dt = 380$ and $dt = 720$, giving a period estimate of around 360 days. The
 415 half-wavelength can be estimated by extending the first maximum line until reaching the
 416 $dt = 0$ axis. This gives $dx = 70^{\circ}$ a wavelength estimate of about 140° . The estimated phase

417 speed is 0.5 m s^{-1} . In the WE region, the zonal velocity anomalies thus show a westward-
 418 propagating signal at an annual period and a basin-scale wavelength ($\sim 140^\circ$), coherent over
 419 at least two years and 15° longitude (Fig. 9a). This confirms the importance of the annual
 420 cycle in this region, taking the form of a Rossby wave, as shown by Cravatte et al. (2012).
 421 The amplitude of the $\text{SSF}_{U'}$ is $400 \text{ cm}^2\text{s}^{-2}$, which corresponds to a wave amplitude of 10
 422 cm s^{-1} (Section 2.2.3), also compatible with Cravatte et al. (2012). The meridional velocity
 423 anomalies also show a westward-propagating signal with a smaller phase speed (0.2 m s^{-1})
 424 and a shorter period (50 days) and wavelength ($\sim 750 \text{ km}$) (Fig. 9b). In addition, the signal
 425 amplitude (3.2 cm s^{-1}) and coherence (<100 days and $<10^\circ$) are much weaker than the
 426 ones for the zonal velocity. This can be caused for example by a time modulation of the
 427 source, or by the presence of a strong vertical component of propagation.

428 Zonal and meridional EKE period estimates from the SSF are consistent with those
 429 from Section 3.2. This shows the consistence of both methods.

430 **3.3.2 Eastern Equatorial Pacific (EE)**

431 In the EE region, a westward propagation of the zonal velocity anomalies at semi-
 432 annual (~ 200 days) periods with a wavelength of 60° , a phase speed of 0.38 m s^{-1} and an
 433 amplitude close to 6 cm s^{-1} is observed (Fig. 10a). Meridional velocity anomalies also have
 434 a westward phase propagation (0.39 m s^{-1}), but at intra-annual period (30 days) and with
 435 a wavelength of 1000 km (Fig. 10b). This signal shows an amplitude of $\sim 4.5 \text{ cm s}^{-1}$ and a
 436 strong phase coherence over at least 20° and 300 days. It is, however, modulated by a low
 437 frequency annual cycle (Fig. 8b shows an intensification at the end of 2016 and beginning
 438 of 2017, during boreal winter time).

439 **3.3.3 North Tropical Pacific (TN)**

440 In the TN region, a westward propagation of meridional velocity anomalies with phase
 441 speed around 0.09 m s^{-1} is observed (Fig. 11a). It is associated with periods of 70 days and
 442 wavelengths of $\sim 500 \text{ km}$. The SSF_V has an amplitude of $\sim 30 \text{ cm}^2\text{s}^{-2}$, which corresponds to
 443 anomalies of amplitude $\sim 3 \text{ cm s}^{-1}$. The signal loses coherence at $dt > 100$ days and $dx > 10^\circ$.

444 **3.3.4 South Tropical Pacific (TS)**

445 The $\text{SSF}_{V'}$ in the TS region shares features with the TN region, including a westward
 446 propagation with phase speed around 0.09 m s^{-1} (Fig. 11b) and similar scales (periods of 70
 447 days and wavelengths of $\sim 500 \text{ km}$). Its amplitude ($14 \text{ cm}^2\text{s}^{-2}$) is, however, much weaker
 448 than in the TN region, as already evidenced from Fig. 4c, and the phase decoherence occurs
 449 at shorter scales. This suggests that although they are energetically important, the waves
 450 or eddies associated with these patterns are very transient and localized, which makes them
 451 difficult to capture.

452 **3.3.5 Pacific Western Boundary (WB)**

453 In the WB region, we performed SSF in the x and in the y direction, but no particular
 454 patterns have been found. This can result from the fact that many different scales are
 455 present and superimposed.

456 **3.3.6 Conclusions**

457 In summary, the variability associated with U' is intensified in the equatorial band and
 458 is found on large scales (annual and semi-annual periods with wavelengths of the order of
 459 the basin scale). The variability associated with V' is found at the Equator and north of
 460 the Equator at shorter scales (periods smaller than 70 days and wavelengths smaller than
 461 1000 km) (Table 2).

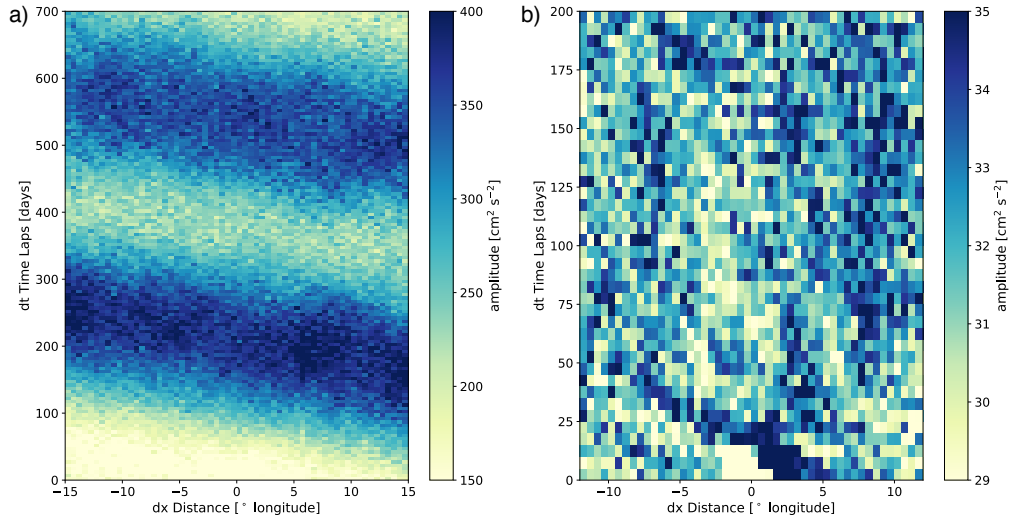


Figure 9. SSF for (a) U' and (b) V' at 1000 m depth in the box EW of Fig 4. All grid cells contain at least 100 realizations.

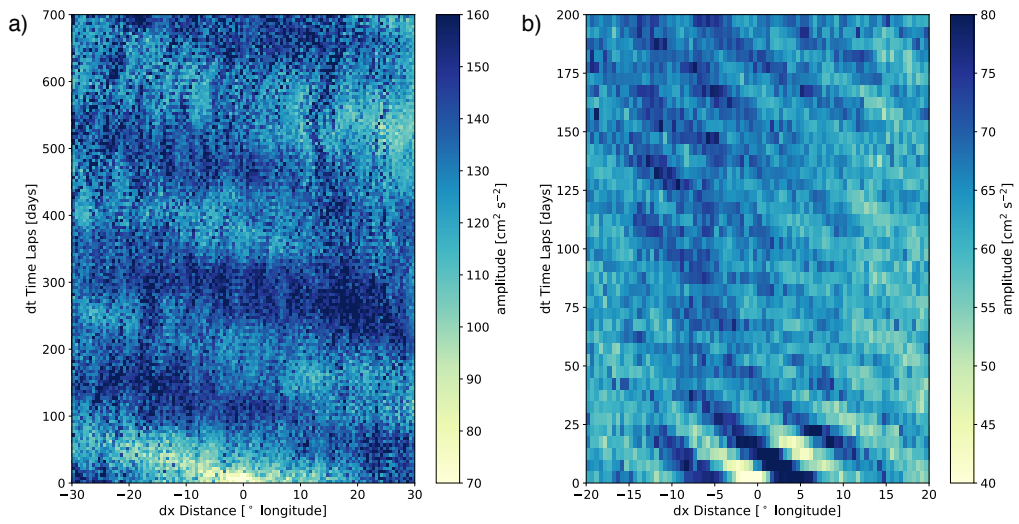


Figure 10. Same as Fig. 9 in the box EE.

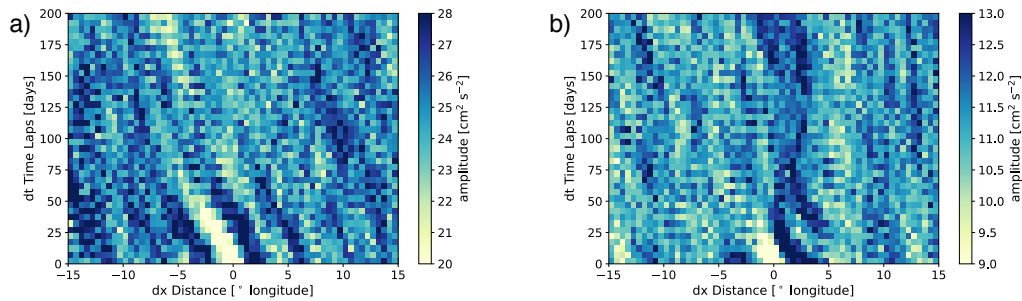


Figure 11. Same as Fig. 9 for V' only in (a) TN and (b) TS.

3.4 Strengthening of EKE at the jet-scale

The aim of this section is to better document the characteristics of the maxima of EKE found in eastward jets (Fig. 5). The method used in the previous sections to estimate the period and wavelength associated with the EKE relies on statistical approaches within large regions (Sections 2.2.2 and 2.2.3). Therefore, it cannot be applied at such a small scale as the jets scale. The approach here is to document and quantify the possible origin of this meridional distribution of EKE.

Distributions of zonal and meridional velocity anomalies, U' and V' , are unimodal in eastward and westward jets (Fig. 12). The standard deviation σ measures the spread of the distribution values. Eastward jets have higher σ (7.1 and 4 for U' and V') than westward jets (5.2 and 2.7 for U' and V'). So velocities reach more frequently extreme values in eastward jets. The eastward to westward standard deviation ratio for V' ($\sigma_e/\sigma_w=1.5$) is stronger than for U' ($\sigma_e/\sigma_w=1.3$), showing a stronger signature of the variability in V' than in U' . In addition, this variability is also associated with a strong signature in EAPE: Fig. 13 shows local maxima of EAPE inside eastward jets, showing that the jet-scale EKE is associated with strong isopycnal fluctuations. All these results suggest the presence of waves or eddies intensified locally inside the eastward jets.

The jet-scale intensified EKE can be generated either locally (through instability of the mean flow for example), or remotely and reach these depths and regions through propagation. For geostrophic flows, barotropic instability occurs when the gradient of potential vorticity changes sign within an isopycnal layer. In this case, the condition can be approximated by a change of sign of $-\partial_{yy}\bar{U} + \beta$, where β is the meridional gradient of the Coriolis parameter (Rayleigh, 1879; Drazin & Howard, 1966; Cushman-Roisin & Beckers, 2011). In the jets, this condition is almost never satisfied, except possibly in the westward jet near 3°S (Fig. 14a). The mean circulation is stable to barotropic perturbations. We thus do not expect the MKE to transfer energy to the EKE locally. The EKE has to come from a remote energy source or other physical processes, such as baroclinic instability.

Conversely, the EKE can have a local effect on the mean flow. The $-\bar{U}\partial_y\overline{U'V'}$ term acts as a source term in the MKE budget (e.g., Gula et al. (2016); Capó et al. (2019)). This term is found to be predominantly positive within 7° of the equator (Fig. 14b), revealing a transfer of energy from EKE to MKE except in the jet near 3°S ($-\bar{U}\partial_y\overline{U'V'} < 0$), where barotropic instability can be active in transferring MKE to EKE (Fig. 14a). The amplitude of the EKE to MKE transfer is roughly $2.10^{-11} \text{ m}^2\text{s}^{-3}$. Given the amplitude of the MKE ($2.5 \times 10^{-3} \text{ m}^2\text{s}^{-2}$ based on a 5 cm s^{-1} mean velocity \bar{U}), the time scale for the EKE to significantly impact the MKE is of order 1000 days, which should remain shorter than the dissipative timescale. In the next section, a potential mechanism that is compatible with the idea of energy transfer from EKE to the mean flow is discussed.

4 Summary and Discussion

Generally zonal velocities are found to vary on large temporal and spatial scales, from semi-annual to annual periods and several thousands of kilometers (Table 2) with a large amplitude that accounts for 64% of the total kinetic energy (not shown). The meridional velocities are found to vary on much shorter temporal and spatial scales at intra-annual periods (30-100 days) and few hundreds of kilometers. When annual variability is filtered out, the zonal velocities also exhibit intra-annual periods, compatible with the meridional velocities off the Equator. The EKE is also larger close to the Equator and tends to decrease poleward, although local maxima are observed, especially in the northern part of the basin.

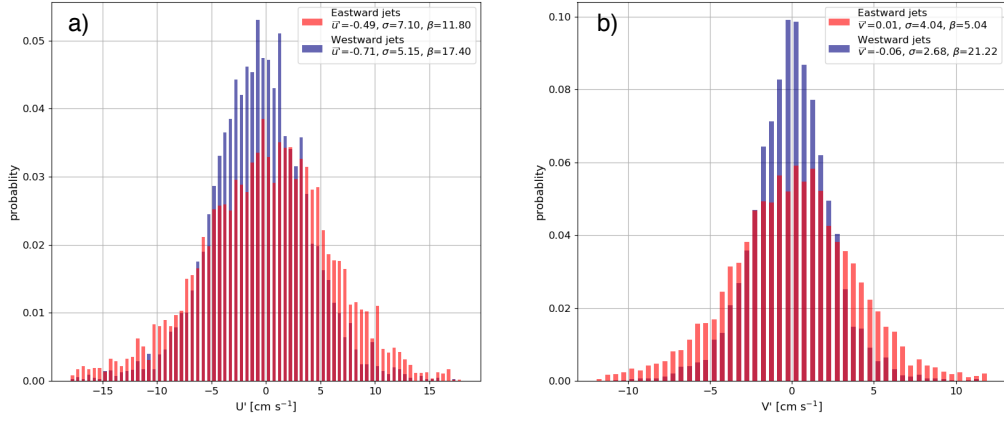


Figure 12. Statistics of (a) U' and (b) V' in eastward jets (red histograms) and westward jets (blue histograms). Histograms are normalized such that the integral over the range is 1. They represent the probability density function at the bin. Statistical indicators are given in the legend. \bar{U}' , \bar{V}' : velocity fluctuations averages, σ : standard deviation, β : kurtosis.

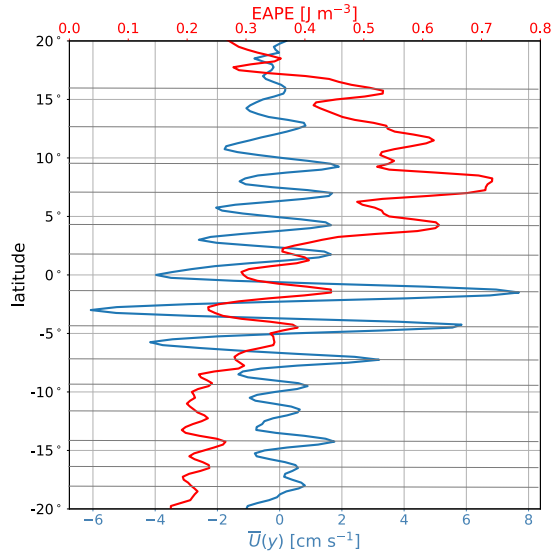


Figure 13. Mean zonal velocity $\bar{U}(y)$ (blue) and EAPE: Eddy Available Potential Energy (red) at 1000 m averaged from 180° to 120°W.

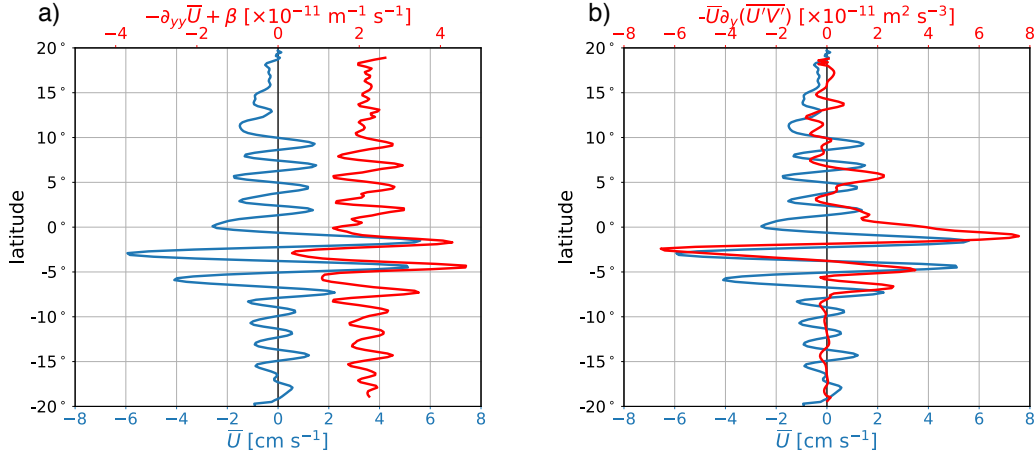


Figure 14. Mean zonal velocity $\bar{U}(y)$ (blue) and (a) Barotropic instability criterion (red); (b) production term in the MKE budget that corresponds to EKE→MKE energy transfer (red) at 1000 m averaged from 180° to 120° W.

508

4.1 Waves propagation and possible generation mechanisms

509

510

511

The aim of this section is to examine how the observed EKE can be consistent with the signature of propagating planetary waves and to discuss their possible generation mechanisms.

We define the non-dimensional parameter M as:

$$M = \frac{Ak^2}{\beta} \quad (14)$$

512

513

514

515

516

517

518

519

520

521

522

523

where A is the amplitude of the variability in zonal or meridional velocity, k its meridional or zonal wavenumber respectively and β the meridional gradient of the Coriolis parameter. M is a measure of the non-linearity of planetary flows (e.g., Gill (1974)). $M \ll 1$ indicates quasi-linear flow and $M \gg 1$ indicates non-linear flow. This parameter is computed in each region using the characteristics found from the scale analysis (Table 2). Note that for U' , the equivalent meridional wave scale is taken as the latitude range length of the regions in which the SSF is applied and can be underestimated. In all regions, $M < 10^{-1}$. This suggests that the deep EKE footprint is more likely to be associated with linear waves than with non-linear eddies. The different scales signature for EKE_U and EKE_V can result from the different KE signature of Equatorial waves. Long waves have indeed higher KE associated with the zonal component of the velocity, while short waves have higher KE associated with the meridional component of the velocity.

524

525

526

527

528

529

530

531

532

533

534

The Equatorial zonal velocity anomalies are associated with annual periods in the western part ($\sim 180^\circ$) of the basin and with semi-annual periods in the eastern part ($\sim 125^\circ$ W). Both scales are compatible with long Rossby waves dispersion relation (Fig. 15). The east-west difference can be explained by the vertical propagation of the energy associated with Equatorial Rossby waves of annual and semi-annual periods. Annual Rossby waves have a shallower ray path and reach 1000 m at about 70° west of their generation site (Fig. 16). If they are generated close to the eastern boundary by reflection of wind-generated equatorial Kelvin waves (as suggested by White (1977)), they are expected to reach 1000 m around 180° , as observed in the western part (EW). Our data also show that annual variability can be present in the middle or eastern part of the basin (Fig. 7b). This is compatible with earlier observations (Kessler & McCreary, 1993; Cravatte et al., 2012) that have detected an-

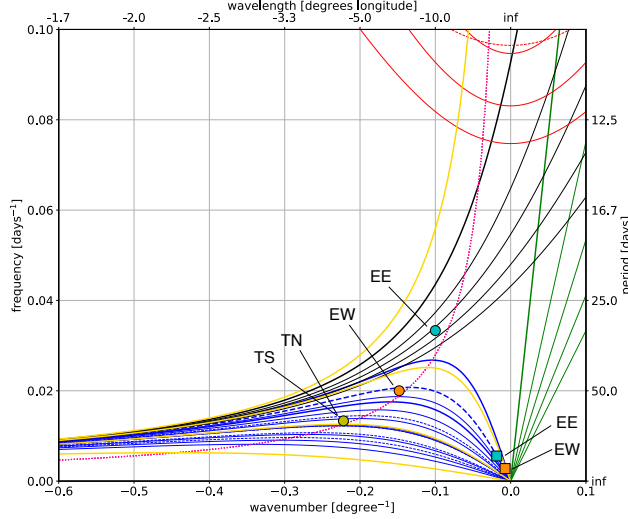


Figure 15. Dispersion relation for Equatorially-trapped and barotropic Rossby waves for a realistic basin-averaged stratification from the climatology CARS (Ridgway & Dunn, 2007). Green: Kelvin waves, Black: Yanai Waves, Red: Inertia-Gravity waves, Blue: Rossby waves. Thick lines : First baroclinic modes. Solid lines: odd meridional modes. Dashed lines : even meridional modes. Yellow: barotropic Rossby wave dispersion relation for $k_y = 0, 10^{-6}, 2 \times 10^{-6}$ and $4 \times 10^{-6} \text{ m}^{-1}$. Colored dots : (k, ω) for V' from estimation in the different regions (Table 2). Colored squares: same for U' .

535 nual Rossby waves at 140°W . This could be explained by the propagation of annual Rossby
 536 waves in the presence of the mean currents (Vallis, 2017). Similarly, semi-annual Rossby
 537 waves reach 1000 m at 40° west of their generation site (Fig. 16). If generated close to the
 538 eastern boundary, they are thus expected around 130°W , a longitude consistent with the
 539 one observed. This supports the idea of vertically-propagating long Rossby waves generated
 540 at the surface close to the eastern boundary. The filtered equatorial zonal velocity, U^* has
 541 periodic fluctuations around 75 days and 120 days (Fig. 7e), which are compatible with
 542 wind-driven Equatorial Kelvin waves as reported from satellite altimetry and subsurface in
 543 situ data analysis (Cravatte et al., 2003).

544 The equatorial meridional velocity anomalies present a strong signal in the spectral
 545 range of the Tropical Instability Waves (TIWs) at 30 days, 1000 km in the eastern part
 546 of the basin. This signal is compatible with high baroclinic mode or vertically-propagating
 547 Yanai waves (Fig. 15). It can be related to the downward propagation of TIWs, as evidenced
 548 from moorings observations in the Atlantic ocean (e.g., Bunge et al. (2008); Von Schuckmann
 549 et al. (2008); Tuchen et al. (2018)). The TIWs in the equatorial Pacific are also associated
 550 with periods of 17 days (Lyman et al., 2007). Although our method does not enable us to
 551 estimate periods shorter than 20 days (Section 2.2.2 and Appendix A), a possible aliasing
 552 of shorter periods cannot be excluded. The phase speed of the V' propagation (Fig. 10)
 553 is compatible with estimates for TIWs (Chelton et al., 2000; Willett et al., 2006). In
 554 addition, TIWs are known to be intensified at the surface from July to November (Willett
 555 et al., 2006). We observe the intensification of the deep TIWs-like signal from September to
 556 February (Fig. 6a). This temporal lag is consistent with the downward energy propagation
 557 time of about 3 months for Yanai waves of period 30 days and wavelength 10° (Fig. 16).
 558 All these elements support the vertical propagation of TIWs at depths of at least 1000
 559 m. In the western part of the basin, waves at 50-day periods and 750-km wavelengths are
 560 observed, matching the dispersion relation for second meridional and first baroclinic mode

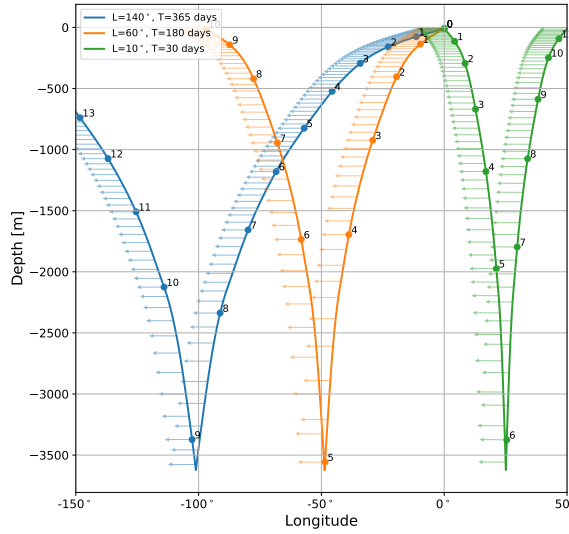


Figure 16. Ray tracing of Equatorial Rossby waves of meridional mode 1 with an annual period (blue line) and semi-annual period (orange line) and of a Yanai wave of period 30 days (green line) initially generated at the surface. The lines indicate the vertical propagation of the energy, they are graduated with a scale of one month (dots), the arrows indicate the phase speed of the wave. The stratification is taken from the climatology CARS (Ridgway & Dunn, 2007) averaged over the entire tropical Pacific.

561 short Rossby waves (Fig. 15). Although they have not been extensively mentioned in the
 562 literature, they are compatible with the observations of Bunge et al. (2008) and Tuchen et
 563 al. (2018) in the Atlantic ocean.

564 The off-equatorial meridional velocity anomalies (poleward of 7°) have a dominant spec-
 565 tral signature at 70 days and 500 km. These spectral characteristics are compatible with the
 566 dispersion relation of barotropic Rossby waves for non-zero meridional wavenumber or high
 567 meridional and baroclinic mode Rossby waves. These characteristics are also compatible
 568 with the presence of westward-propagating eddies with diameters of 200-250 km, which is
 569 the typical scale expected at these latitudes (Chelton et al., 2011; Yang et al., 2013). An
 570 important source of eddy generation is located along the central America coast, where the
 571 wind form eddies of diameter around 150-300 km, that propagate further west at speeds
 572 of $5\text{-}15\text{ cm s}^{-1}$ (Stumpf & Legeckis, 1977; Willett et al., 2006; Kurczyn et al., 2012). The
 573 distinction on the nature (waves or eddies) of the observed anomalies at depth is not triv-
 574 ial. Several arguments however, would support that these anomalies are associated with
 575 waves rather than eddies. The non-linearity parameter is of order 10^{-1} (Table 2) and the
 576 signal is found to be coherent over the latitudinal extent of the TN region, that is at least 7°
 577 (Fig. 11). This meridional coherence suggests large meridional scale anomalies. This is com-
 578 patible with the presence of barotropic Rossby waves, which are not equatorially-trapped
 579 and can have large meridional extent. Farrar (2011) noted the presence of barotropic Rossby
 580 waves radiating from the TIWs and reaching 20° . However, the period and wavelength he
 581 measured are not compatible with those observed here. The question of the origin of these
 582 waves remains. Some evidence of waves generated by barotropic and baroclinic instabil-
 583 ities of surface currents is given by Farrar and Weller (2006) from observations at 10°N ,
 584 125°W in the tropical Pacific, and by Tchilibou (2018) from a realistic mesoscale resolv-

585 ing simulation of the tropical Pacific. In the latter study, the author shows that in the
 586 North Tropical Pacific, the shear and density gradient between the westward NEC and the
 587 eastward Subtropical Counter Current (STCC) and Hawaiian Lee Counter Current (HLCC)
 588 (Fig. 1) generate barotropic and baroclinic instabilities. A spectral energy budget shows
 589 that baroclinic instability produces EKE at intra-seasonal periods (close to 50 days) and
 590 short wavelengths (300km). Barotropic instability is smaller but produces EKE at 100-day
 591 periods and 400-km wavelengths.

592 **4.2 A link with the formation and maintenance of the mean jet-structured** 593 **circulation ?**

594 Our study gives some insight into the possible origin of the mean deep circulation,
 595 with its alternating zonal jets. The maxima of meridional variability (Fig. 5b) and EAPE
 596 (Fig. 13) in eastward jets is inconsistent with the eddy-averaging hypothesis (Berloff et al.,
 597 2011), which would lead to maxima between the jets. Several studies have shown that waves,
 598 and in particular short intra-annual waves, are a possible energy source for the mean deep
 599 Equatorial circulation. They efficiently propagate energy downward because of their steep
 600 ray paths (Cox, 1980) and they are prone to instabilities that develop jet-like structures
 601 (Hua et al., 2008; Ménesguen et al., 2009). Forcing a numerical simulation with a wave
 602 maker of 50-day period at the Equator, Ménesguen et al. (2009) were able to reproduce the
 603 near-equatorial jets within the 3°S-3°N latitude range. Similarly, Ascani et al. (2010) were
 604 able to reproduce meridionally-alternating jet-like structures in the near-equatorial band by
 605 forcing a vertically-propagating Yanai wave beam at 30-day period and 1000-km wavelength.
 606 The short waves (periods <100 days and wavelengths <1000 km) observed in this study at
 607 the Equator and off the Equator at 1000 m depth give some observational evidence for the
 608 energy sources required by this mechanism.

609 The modulation of the EKE and EAPE intensity at the jet scale with higher EKE and
 610 EAPE inside eastward jets is compatible with a process called 'jet sharpening' that might
 611 help maintain these jets (Dritschel & McIntyre, 2008; Dritschel & Scott, 2011). The presence
 612 of the jets lead to a modification of the background potential vorticity gradient, shaped as a
 613 staircase profile with fronts inside eastward jets (Delpech et al., 2020). The jet-sharpening
 614 theory predicts that these potential vorticity staircases will modify the Rossby elasticity
 615 and favor a wave regime inside the eastward jets (as Rossby waves need a potential vorticity
 616 gradient to propagate) and a turbulent regime inside westward jets. This dual regime
 617 maintains the potential vorticity staircases and thus the jets themselves. Therefore, we can
 618 expect the wave dynamical signal to be intensified in regions of strong potential vorticity
 619 gradients. The Argo observations provide a 10-day low pass filtered EKE, that will more
 620 likely capture the wave regime than the high frequency turbulent mixing. The observations
 621 of higher EKE and EAPE within eastward jets (Fig. 5 and 13) are thus consistent with the
 622 jet-sharpening theory. Another consequence of the presence of jets and varying background
 623 potential vorticity gradients is the local modification of the phase speed of the wave. This
 624 deforms waves fronts and can create a convergence of energy flux (Greatbatch et al., 2018)
 625 and a transfer of energy towards the mean flow (MKE), as evidenced from Fig. 14b.

626 To conclude, observations of intensified EKE and APE along eastward jets are consis-
 627 tent with a variability associated with propagating Rossby waves whose structure is locally
 628 modified by the deep jets structure. They can also possibly support the jet sharpening
 629 mechanism. These results remain qualitative and a full understanding of the mechanisms
 630 would require numerical simulations that are beyond the scope of this study.

631 **4.3 Perspectives**

632 This study provides the first basin-scale description of the 1000 m EKE, from La-
 633 grangian float displacements. Although the analysis of this unique database has provided

634 new insight into the spatial and temporal variability of currents at 1000 m, it is, like all
635 observational analyses, limited by the characteristics of the observations.

636 One limitation arises from the temporal and spatial sampling of the Argo drifts. Dur-
637 ing the 2014-2018 period when sampling was most frequent, there were an average of 10
638 measurements per square degree per year. To retain robust statistics, we were unable to
639 choose a region that is too narrow as this limits the number of measurements. For this
640 reason, the scale analysis could not be refined to characterize the scales of energy in small
641 localized regions (as inside jets). However, the increasing number of floats over time, and
642 the recommendation of doubling Argo density in the equatorial ocean (Smith et al., 2019)
643 should allow higher resolution in future studies.

644 Another limitation is imposed by the quasi-Lagrangian nature of the Argo drift veloc-
645 ities. Ideally, a systematic method to correct the Doppler shift would allow us to estimate
646 the wavenumber and frequency of the EKE with a good precision for each float and would
647 thus provide a local information about the different scales of variability, as well as their spa-
648 tial and temporal variations. Such corrections are however not straightforward and often
649 require strong assumptions (Barbot et al., 2018). No appropriate method exists to date and
650 this would deserve a full investigation in future studies.

651 Finally, although the methodology developed in this study has been applied to provide
652 a description of the spectral content at 1000 m depth only, it will hopefully be useful to
653 investigate the energy scale dependence at other depths. In particular, a comparison with the
654 scale dependence of surface variability, using for example drifters velocities, in combination
655 with theoretical energy ray tracing would help determining which part of the observed deep
656 spectrum is surface driven and which part is internally driven. In addition, a more thorough
657 analysis of the vertical energy propagation using the EAPE at the different depths would
658 be valuable as an attempt to address the question of the vertical energy propagation in the
659 equatorial regions.

Table 1. YoMaHA database statistics of 1000 m velocity estimates in the tropical Pacific basin for the whole Argo period 1997-2019. trp. Pacific: 120°E-70°W, 20°S-20°N. EW: 165°E-175°W, 3°S-3°N. EE: 155°W-90°W, 3°S-3°N. TN: 170°E-125°W, 7°N-17°N. TS: 160°W-90°W, 7°S-17°S, WB: 125°E-135°E, 0°-17°N (Fig 4). The average lifetime (avg. lifetime) represents the averaged time spent by each float in a given region. The average x-distance (avg. x-dist) and (avg. y-dist) y-distance represent the averaged maximal zonal and meridional extension of each float trajectory in a given region. The number of synchronous measurements (# synchron.) represents the mean number of measurements in the region per time intervals of 10 days and the number of climatological measurements (# clim.) represents the minimal number of measurements per climatological month used to construct the U^m field (Eq. 3).

	# floats	# measurements	avg. lifetime (days)	avg. x-dist (° lon)	avg. y-dist (° lat)	# synchron.	# clim.
trp. Pacific	1879	256139	1416	16.5	4.0	179	19994
EW	172	8237	656	13.9	1.9	7	405
EE	267	21278	903	15.5	2.2	18	1236
TS	451	46079	1160	11.6	2.5	34	1233
TN	402	45782	1325	15.6	3.3	35	1009
WB	89	7735	755	9.2	4.2	9	142

Table 2. Summary of characteristic scales found in each region defined in Fig. 4 for the zonal velocity (U), the meridional velocity (V) and the zonal velocity minus the seasonal cycle (U^*). The seasonal cycle is mostly present in the 5°S - 5°N band, U^* is thus computed for the EE and EW regions only. T is the period, λ the wavelength, A the amplitude, c_φ the phase speed and $M = \frac{Ak^2}{\beta}$, where $k = \frac{2\pi}{\lambda}$ is the wavenumber (equivalent meridional wavenumber for U and zonal wavenumber for V). Note that the equivalent meridional wavenumber can only be overestimated such that M for U is an upper bound. β is the meridional gradient of the Coriolis parameter, is a non-dimensional parameter that measures the non-linearity of the flow. $M \ll 1$ indicates a weak non-linearity, the variability can be associated with waves, $M \gg 1$ indicates a strong non-linearity, the variability can be associated with eddies.

	U'					V'					U^*
	T (day)	λ (km)	A (cm.s^{-1})	c_φ (m.s^{-1})	M (-)	T (day)	λ (km)	A (cm.s^{-1})	c_φ (m.s^{-1})	M (-)	T (day)
• EE	180	~ 6000	6.3	0.38	$\leq 3.10^{-3}$	30	~ 1000	4.5	0.39	7.10^{-2}	120
• EW	360	~ 15000	10	0.5	$\leq 5.10^{-3}$	50	750	3.5	0.2	1.10^{-1}	120
• TN	360	-	-	-	-	70	500	3	0.09	2.10^{-1}	70
• TS	360	-	-	-	-	70	500	1.5	0.09	1.10^{-1}	-
• WB	360	-	-	-	-	~ 60	-	-	-	-	~ 80

Appendix A Wavelet Analysis validation: Doppler Shift influence on period estimation

The purpose of this appendix is to quantify the error made on the estimation of the period by neglecting the Doppler shift. We perform experiments with a single synthetic float. The synthetic float is advected in a prescribed wave field with a background mean flow. The positions of the float are then subsampled every 10 days along its trajectory and the velocities are estimated using the differential positions to reconstruct an Argo-like dataset. The period of the wave is then estimated by performing a wavelet analysis on the float velocity time series. The estimated period (\hat{P}) is then compared with the true period of the wave (P) for different waves and background mean flow velocities.

For all the experiments, we consider a plane wave propagating along the zonal direction with a wavenumber k and a frequency ω , and a zonal background mean flow \bar{u}_0 . The float is thus advected in the Eulerian velocity field given by Eq A1:

$$\begin{cases} u = \bar{u}_0 \\ v = v_0 \sin(kx - \omega t) \end{cases} \quad (\text{A1})$$

A first experiment with $\bar{u}_0 = 0$ shows that every period larger than the period corresponding to the Nyquist frequency can be estimated with very little error (Fig. A1). There is little influence of taking the 10-day averaged velocities as instantaneous velocities and the Lagrangian time series as an Eulerian time series. This ensures that the method described in Section 2.2.2 is valid in spite of the two first approximations made.

Three other experiments with $\bar{u}_0 = 2, 4$ and 6 cm s^{-1} are performed. In practice the deep mean flow in the tropical oceans is mainly zonal and does not exceed $6\text{-}8 \text{ cm s}^{-1}$ (eg., Fig. 5). These experiments are thus representative of realistic conditions. The wave period is estimated with a greater error compared to the true period as the background mean flow velocity increases. The error increases also with the period and depends on the wavelength.

More generally, the error increases as the background mean velocity approaches the phase speed of the wave (Fig. A2). The error is "linear" with the velocity sign: for positive waves phase speed, a positive background mean flow leads to an overestimation of the wave period and a negative background mean flow leads to underestimation of the wave period. For high phase speed waves (Fig. A2b), the error remains small (because the mean flow will never reach the phase speed) and when periods are averaged over a region large enough to encompass both eastward and westward jets, the individual error might compensate and give a good estimate for the period. For low phase speed waves however, the error can be as large as the wave period. In this study, it has been checked that the waves phase speeds are always large compared to the mean currents, so that the calculated periods are reliable.

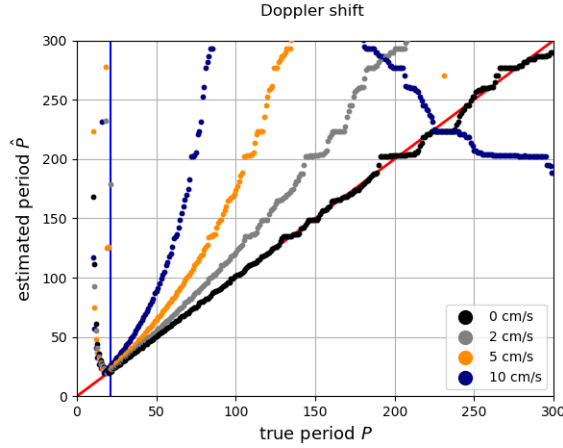


Figure A1. Period estimated by the wavelet analysis method as a function of the true period. The velocity time series are reconstructed following the Argo protocol: the float is advected with a high resolution Eulerian velocity field, the trajectory is subsampled at a 10-day sampling period and the velocity time series is reconstructed from the differential float positions. Each color corresponds to a background mean flow velocity amplitude. The wave has a wavelength of 1000 km. The blue line indicates the period corresponding to the Nyquist frequency, and the red line indicates the first bisector $y = x$ where the estimated period fits the true period.

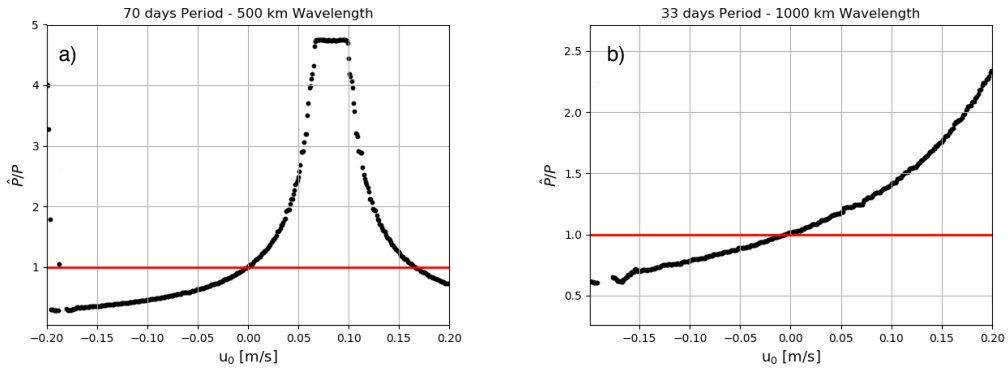


Figure A2. Ratio of estimated period to the true period as a function of the mean zonal velocity u_0 for a (a) (70 days, 500 km, $c_\varphi = 0.08$) wave and (b) (33 days, 1000 km, $c_\varphi = 0.35$) TIW-like wave. The red line corresponds to a ratio of 1 where the estimated period fits the true period. A maximum of the error on the estimated period is reached when the velocity u_0 matches the phase speed of the wave.

Appendix B Statistical Scales Functions (SSF) validation

The purpose of this appendix is to validate the statistical method developed in Section 2.2.3 to infer waves properties (period, wavelength and amplitude) from random velocity measurements at depth. We perform experiments with synthetic floats within a prescribed wave field. We numerically advect 50 synthetic floats during three years with random start dates and positions in an idealized wave velocity field with a superimposed zonal current given by Eq. B1. The float positions are subsampled every 10 days along the trajectories.

$$\begin{cases} u = \bar{u}_0 + v_0 \sin(kx - \omega t) \\ v = v_0 \cos(kx - \omega t) \end{cases} \quad (\text{B1})$$

where k is the wavenumber, ω the period and v_0 the amplitude of the wave. The background mean flow is set to $\bar{u}_0 = 5 \text{ cm s}^{-1}$. The velocity are estimated using the differential positions in order to reconstruct an Argo-like dataset ($U_{\text{syn}}, V_{\text{syn}}$). The $\text{SSF}_{U_{\text{syn}}}$ and $\text{SSF}_{V_{\text{syn}}}$ are then computed as described in Section 2.2.3.

Two experiments with a period of 70 days, a wavelength of 500 km and amplitudes of 3 cm s^{-1} (Fig. B1a) and 10 cm s^{-1} (Fig. B1b) are tested. In Fig. B1 only the $\text{SSF}_{V_{\text{syn}}}$ is shown but the $\text{SSF}_{U_{\text{syn}}}$ is identical.

The period and wavelength of the wave are estimated with a good precision. In particular, this method is not sensitive to the Doppler shift (even in the case where the amplitude of the wave is small compared to the background current). As expected, the amplitude of the SSF varies with the amplitude of the wave. However, the estimated amplitude (2.5 cm s^{-1} for the first experiment and 7 cm s^{-1} for the second one) is slightly underestimated. This can be due to the 10-day average resulting from the dataset construction (Lebedev et al., 2007). This average acts as a boxcar low-pass filter that can yield significant attenuation, even for frequency a bit lower than the filter length. The SSF is therefore a very powerful tool to measure the spectral signature of the signal provided by the Argo floats, although the amplitudes estimated from the SSF can be underestimated.

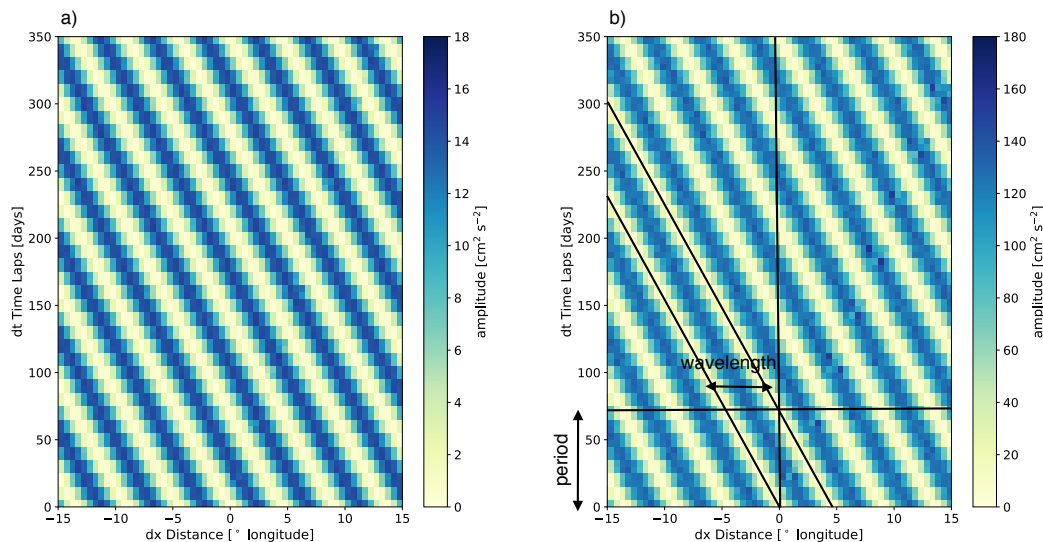


Figure B1. SSF for a synthetic floats in an analytical wave field of period 70 days, wavelength 500 km and amplitudes of (a) 3 cm s^{-1} and (b) 10 cm s^{-1} .

Acknowledgments

This study used the data of YoMaHA'07 (Lebedev et al., 2007) dataset of velocities derived from Argo float trajectories provided by APDRC/IPRC, available at <http://apdrc.soest.hawaii.edu/projects/yomaha/> (last accessed 09/04/2020). The authors are grateful to G. Roulet who provided the EAPE dataset, available at: <https://www.seanoe.org/data/00612/72432/> (last accessed: 09/04/2020). This work benefited from fruitful discussions with G. Serazin, M. Tchilibou, S. Barbot and J. Gula. The authors are also grateful to N. Hall for the grammatical corrections and to E. Firing and one anonymous reviewer for their insightful comments that have improved the quality of the manuscript.

References

- Ascani, F., Firing, E., Dutrieux, P., McCreary, J. P., & Ishida, A. (2010). Deep equatorial ocean circulation induced by a forced-dissipated yanai beam. *J. Phys. Oceanogr.*, *40*(5), 1118–1142.
- Ascani, F., Firing, E., McCreary, J. P., Brandt, P., & Greatbatch, R. J. (2015). The deep equatorial ocean circulation in wind-forced numerical solutions. *J. Phys. Oceanogr.*, *45*(6), 1709–1734.
- Babiano, A., Basdevant, C., & Sadourny, R. (1985). Structure functions and dispersion laws in two-dimensional turbulence. *Journal of the atmospheric sciences*, *42*(9), 941–949.
- Balwada, D., LaCasce, J. H., & Speer, K. G. (2016). Scale-dependent distribution of kinetic energy from surface drifters in the gulf of mexico. *Geophysical Research Letters*, *43*(20), 10–856.
- Barbot, S., Petrenko, A., & Maes, C. (2018). Intermediate water flows in the western south pacific: as revealed by individual argo floats trajectories and a model re-analysis. *Biogeosciences*, *15*(13), 4103–4124. Retrieved from <https://www.biogeosciences.net/15/4103/2018/> doi: 10.5194/bg-15-4103-2018
- Bastin, S., Claus, M., Brandt, P., & Greatbatch, R. J. (2020). Equatorial deep jets and their influence on the mean equatorial circulation in an idealized ocean model forced by intraseasonal momentum flux convergence. *Geophysical Research Letters*, *47*(10), e2020GL087808. doi: 10.1029/2020GL087808

- 744 Berloff, P., Karabasov, S., Farrar, J. T., & Kamenkovich, I. (2011). On latency of multiple
745 zonal jets in the oceans. *Journal of Fluid Mechanics*, *686*, 534–567.
- 746 Bunge, L., Provost, C., Hua, B. L., & Kartavtseff, A. (2008). Variability at intermediate
747 depths at the equator in the atlantic ocean in 2000–06: Annual cycle, equatorial deep
748 jets, and intraseasonal meridional velocity fluctuations. *Journal of Physical Oceanog-*
749 *raphy*, *38*(8), 1794–1806.
- 750 Capó, E., Orfila, A., Mason, E., & Ruiz, S. (2019). Energy conversion routes in the western
751 mediterranean sea estimated from eddy–mean flow interactions. *Journal of Physical*
752 *Oceanography*, *49*(1), 247–267.
- 753 Chelton, D. B., Schlax, M. G., & Samelson, R. M. (2011). Global observations of nonlinear
754 mesoscale eddies. *Progress in oceanography*, *91*(2), 167–216.
- 755 Chelton, D. B., Wentz, F. J., Gentemann, C. L., de Szoeke, R. A., & Schlax, M. G. (2000).
756 Satellite microwave sst observations of transequatorial tropical instability waves. *Geo-*
757 *physical Research Letters*, *27*(9), 1239–1242.
- 758 Contreras, R. F. (2002). Long-term observations of tropical instability waves. *Journal of*
759 *Physical Oceanography*, *32*(9), 2715–2722.
- 760 Cox, M. D. (1980). Generation and propagation of 30-day waves in a numerical model of
761 the pacific. *Journal of Physical Oceanography*, *10*(8), 1168–1186.
- 762 Cravatte, S., Kessler, W. S., & Marin, F. (2012). Intermediate zonal jets in the tropical
763 pacific ocean observed by argo floats. *J. Phys. Oceanogr.*, *42*(9), 1475–1485.
- 764 Cravatte, S., Kestenare, E., Marin, F., Dutrieux, P., & Firing, E. (2017). Subthermo-
765 cline and intermediate zonal currents in the tropical pacific ocean: Paths and vertical
766 structure. *J. Phys. Oceanogr.*, *47*(9), 2305–2324.
- 767 Cravatte, S., Picaut, J., & Eldin, G. (2003). Second and first baroclinic kelvin modes in
768 the equatorial pacific at intraseasonal timescales. *Journal of Geophysical Research:*
769 *Oceans*, *108*(C8).
- 770 Cushman-Roisin, B., & Beckers, J.-M. (2011). *Introduction to geophysical fluid dynamics:*
771 *physical and numerical aspects*. Academic press.
- 772 Delpech, A., Cravatte, S., Marin, F., Morel, Y., Gronchi, E., & Kestenare, E. (2020).
773 Observed tracer fields structuration by middepth zonal jets in the tropical pacific.
774 *Journal of Physical Oceanography*, *50*(2), 281–304.
- 775 Drazin, P., & Howard, L. (1966). Hydrodynamic stability of parallel flow of inviscid fluid.
776 In *Advances in applied mechanics* (Vol. 9, pp. 1–89). Elsevier.
- 777 Dritschel, D., & McIntyre, M. (2008). Multiple jets as pv staircases: the phillips effect and
778 the resilience of eddy-transport barriers. *Journal of the Atmospheric Sciences*, *65*(3),
779 855–874.
- 780 Dritschel, D., & Scott, R. (2011). Jet sharpening by turbulent mixing. *Philosophical Trans-*
781 *actions of the Royal Society A: Mathematical, Physical and Engineering Sciences*,
782 *369*(1937), 754–770.
- 783 Eriksen, C. C., & Richman, J. G. (1988). An estimate of equatorial wave energy flux at
784 9-to 90-day periods in the central pacific. *Journal of Geophysical Research: Oceans*,
785 *93*(C12), 15455–15466.
- 786 Farrar, J. T. (2011). Barotropic rossby waves radiating from tropical instability waves in
787 the pacific ocean. *Journal of Physical Oceanography*, *41*(6), 1160–1181.
- 788 Farrar, J. T., & Durland, T. S. (2012). Wavenumber–frequency spectra of inertia–gravity
789 and mixed rossby–gravity waves in the equatorial pacific ocean. *Journal of physical*
790 *oceanography*, *42*(11), 1859–1881.
- 791 Farrar, J. T., & Weller, R. A. (2006). Intraseasonal variability near 10 n in the eastern
792 tropical pacific ocean. *Journal of Geophysical Research: Oceans*, *111*(C5).
- 793 Firing, E., Kashino, Y., & Hacker, P. (2005). Energetic subthermocline currents observed
794 east of mindanao. *Deep Sea Research Part II: Topical Studies in Oceanography*, *52*(3-
795 4), 605–613.
- 796 Gill, A. (1974). The stability of planetary waves on an infinite beta-plane. *Geophysical and*
797 *Astrophysical Fluid Dynamics*, *6*(1), 29–47.
- 798 Gouriou, Y., Delcroix, T., & Eldin, G. (2006). Upper and intermediate circulation in the

- 799 western equatorial pacific ocean in october 1999 and april 2000. *Geophys. Res. Lett.*,
800 33(10).
- 801 Greatbatch, R. J., Claus, M., Brandt, P., Matthießen, J.-D., Tuchen, F. P., Ascani, F.,
802 ... Farrar, J. T. (2018). Evidence for the maintenance of slowly varying equatorial
803 currents by intraseasonal variability. *Geophysical Research Letters*, 45(4), 1923–1929.
- 804 Gula, J., Molemaker, M. J., & McWilliams, J. C. (2016). Topographic generation of
805 submesoscale centrifugal instability and energy dissipation. *Nature communications*,
806 7(1), 1–7.
- 807 Hua, B. L., D’Orgeville, M., Fruman, M. D., Menesguen, C., Schopp, R., Klein, P., &
808 Sasaki, H. (2008). Destabilization of mixed rossby gravity waves and the formation
809 of equatorial zonal jets. *J. Fluid Mech.*, 610, 311–341.
- 810 Kessler, W. S., & McCreary, J. P. (1993). The annual wind-driven rossby wave in the
811 subthermocline equatorial pacific. *Journal of Physical Oceanography*, 23(6), 1192–
812 1207.
- 813 Kurczyn, J., Beier, E., Lavín, M., & Chaigneau, A. (2012). Mesoscale eddies in the north-
814 eastern pacific tropical-subtropical transition zone: Statistical characterization from
815 satellite altimetry. *Journal of Geophysical Research: Oceans*, 117(C10).
- 816 Lagerloef, G. S., Mitchum, G. T., Lukas, R. B., & Niiler, P. P. (1999). Tropical pacific
817 near-surface currents estimated from altimeter, wind, and drifter data. *Journal of*
818 *Geophysical Research: Oceans*, 104(C10), 23313–23326.
- 819 Lebedev, K. V., Yoshinari, H., Maximenko, N. A., & Hacker, P. W. (2007). Velocity data
820 assessed from trajectories of argo floats at parking level and at the sea surface.
- 821 Lee, G., Gommers, R., Waselewski, F., Wohlfahrt, K., & O’Leary, A. (2019). Pywavelets: A
822 python package for wavelet analysis. *Journal of Open Source Software*, 4(36), 1237.
- 823 Legeckis, R. (1977). Long waves in the eastern equatorial pacific ocean: A view from a
824 geostationary satellite. *Science*, 197(4309), 1179–1181.
- 825 Lindstrom, E., Bourassa, M., Chelton, D., Corlett, G., Durland, T., Farrar, T., ... others
826 (2014). White paper# 9–satellite views of the tropical pacific.
- 827 Lukas, R., & Firing, E. (1985). The annual rossby wave in the central equatorial pacific
828 ocean. *Journal of physical oceanography*, 15(1), 55–67.
- 829 Lyman, J. M., Chelton, D. B., DeSzoeko, R. A., & Samelson, R. M. (2005). Tropical
830 instability waves as a resonance between equatorial rossby waves. *Journal of physical*
831 *oceanography*, 35(2), 232–254.
- 832 Lyman, J. M., Johnson, G. C., & Kessler, W. S. (2007). Distinct 17-and 33-day tropical
833 instability waves in subsurface observations. *Journal of physical oceanography*, 37(4),
834 855–872.
- 835 Marin, F., Kestenare, E., Delcroix, T., Durand, F., Cravatte, S., Eldin, G., & Bourdalle-
836 Badie, R. (2010). Annual reversal of the equatorial intermediate current in the pacific:
837 Observations and model diagnostics. *J. Phys. Oceanogr.*, 40(5), 915–933.
- 838 McCaffrey, K., Fox-Kemper, B., & Forget, G. (2015). Estimates of ocean macroturbulence:
839 Structure function and spectral slope from argo profiling floats. *Journal of Physical*
840 *Oceanography*, 45(7), 1773–1793.
- 841 McPhaden, M. J. (1996). Monthly period oscillations in the pacific north equatorial coun-
842 tercurrent. *Journal of Geophysical Research: Oceans*, 101(C3), 6337–6359.
- 843 Ménesguen, C., Delpech, A., Marin, F., Cravatte, S., Schopp, R., & Morel, Y. (2019). Obser-
844 vations and mechanisms for the formation of deep equatorial and tropical circulation.
845 *Earth and Space Science*.
- 846 Ménesguen, C., Hua, B. L., Fruman, M. D., & Schopp, R. (2009). Dynamics of the combined
847 extra-equatorial and equatorial deep jets in the atlantic. *J. Mar. Res.*, 67(3), 323–346.
- 848 Morel, P., & Larcheveque, M. (1974, 10). Relative dispersion of constant-level balloons in
849 the 200-mb general circulation. *Journal of Atmospheric Sciences*, 31, 2189–2196.
- 850 Ollitrault, M., & Colin de Verdière, A. (2014). The ocean general circulation near 1000-m
851 depth. *J. Phys. Oceanogr.*, 44(1), 384–409.
- 852 Ollitrault, M., Lankhorst, M., Fratantoni, D., Richardson, P., & Zenk, W. (2006). Zonal
853 intermediate currents in the equatorial atlantic ocean. *Geophys. Res. Lett.*, 33(5).

- 854 Ollitrault, M., & Rannou, J.-P. (2013). Andro: An argo-based deep displacement dataset.
855 *Journal of Atmospheric and Oceanic Technology*, *30*(4), 759–788.
- 856 Philander, S. (1978). Instabilities of zonal equatorial currents, 2. *Journal of Geophysical*
857 *Research: Oceans*, *83*(C7), 3679–3682.
- 858 Qiu, B., Rudnick, D. L., Chen, S., & Kashino, Y. (2013). Quasi-stationary north equatorial
859 undercurrent jets across the tropical north pacific ocean. *Geophysical Research Letters*,
860 *40*(10), 2183–2187.
- 861 Rayleigh, L. (1879). On the stability, or instability, of certain fluid motions. *Proceedings of*
862 *the London Mathematical Society*, *1*(1), 57–72.
- 863 Ridgway, K., & Dunn, J. (2007). Observational evidence for a southern hemisphere oceanic
864 supergyre. *Geophysical Research Letters*, *34*(13).
- 865 Roemmich, D., Alford, M. H., Claustre, H., Johnson, K., King, B., Moum, J., ... others
866 (2019). On the future of argo: A global, full-depth, multi-disciplinary array. *Frontiers*
867 *in Marine Science*, *6*.
- 868 Roulet, G. (2020). World ocean atlas of argo inferred statistics.
869 doi: 10.1.1/jpb001
- 870 Roulet, G., Capet, X., & Maze, G. (2014). Global interior eddy available potential energy
871 diagnosed from argo floats. *Geophysical Research Letters*, *41*(5), 1651–1656.
- 872 Sérazin, G., Marin, F., Gourdeau, L., Cravatte, S., Morrow, R., & Dabat, M.-L. (2020).
873 Scale-dependent analysis of in situ observations in the mesoscale to submesoscale
874 range around new caledonia. *Ocean Science Discussions*, *2019*, 1–32. Retrieved from
875 <https://www.ocean-sci-discuss.net/os-2019-124/> doi: 10.5194/os-2019-124
- 876 Smith, N., Kessler, W. S., Cravatte, S., Sprintall, J., Wijffels, S., Cronin, M. F., ... others
877 (2019). Tropical pacific observing system. *Frontiers in Marine Science*, *6*, 31.
- 878 Stumpf, H. G., & Legeckis, R. V. (1977). Satellite observations of mesoscale eddy dynamics
879 in the eastern tropical pacific ocean. *Journal of Physical Oceanography*, *7*(5), 648–658.
- 880 Tchilibou, M. L. (2018). *Dynamique méso-sous-méso-échelle et marée interne dans le paci-*
881 *fique tropical: implications pour l’altimétrie et la mer des salomon* (Unpublished doc-
882 toral dissertation).
- 883 Torrence, C., & Compo, G. P. (1998). A practical guide to wavelet analysis. *Bulletin of the*
884 *American Meteorological society*, *79*(1), 61–78.
- 885 Tuchen, F. P., Brandt, P., Claus, M., & Hummels, R. (2018). Deep intraseasonal variability
886 in the central equatorial atlantic. *Journal of Physical Oceanography*, *48*(12), 2851–
887 2865.
- 888 Vallis, G. K. (2017). *Atmospheric and oceanic fluid dynamics*. Cambridge University Press.
- 889 Von Schuckmann, K., Brandt, P., & Eden, C. (2008). Generation of tropical instability
890 waves in the atlantic ocean. *Journal of Geophysical Research: Oceans*, *113*(C8).
- 891 Wang, F., Li, Y., & Wang, J. (2016). Intraseasonal variability of the surface zonal currents
892 in the western tropical pacific ocean: Characteristics and mechanisms. *Journal of*
893 *Physical Oceanography*, *46*(12), 3639–3660.
- 894 Weber, J. E. H. (2017). Equatorial Stokes drift and Rossby rip currents. *Journal of*
895 *Geophysical Research: Oceans*, *122*(6), 4819–4828.
- 896 White, W. B. (1977). Annual forcing of baroclinic long waves in the tropical north pacific
897 ocean. *Journal of Physical Oceanography*, *7*(1), 50–61.
- 898 Willett, C. S., Leben, R. R., & Lavín, M. F. (2006). Eddies and tropical instability waves in
899 the eastern tropical pacific: A review. *Progress in Oceanography*, *69*(2-4), 218–238.
- 900 Wyrki, K., & Kilonsky, B. (1984). Mean water and current structure during the hawaii-
901 to-tahiti shuttle experiment. *Journal of Physical Oceanography*, *14*(2), 242–254.
- 902 Yang, G., Wang, F., Li, Y., & Lin, P. (2013). Mesoscale eddies in the northwestern
903 subtropical pacific ocean: Statistical characteristics and three-dimensional structures.
904 *Journal of Geophysical Research: Oceans*, *118*(4), 1906–1925.
- 905 Zanowski, H., Johnson, G. C., & Lyman, J. M. (2019). Equatorial pacific 1,000-dbar
906 velocity and isotherm displacements from argo data: Beyond the mean and seasonal
907 cycle. *Journal of Geophysical Research: Oceans*.

908 Zhang, Z., Pratt, L. J., Wang, F., Wang, J., & Tan, S. (2020). Intermediate intraseasonal
909 variability in the western tropical pacific ocean: meridional distribution of equato-
910 rial rossby waves influenced by a tilted boundary. *Journal of Physical Oceanogra-*
911 *phy*(2020).